

AD # Not IN DTIC

ESD-TR-77-44

DRI File Copy

# ESD ACCESSION LIST

DRI Call No. 86 812

Copy No. 1 of 2 cys.

1

Solid State Research

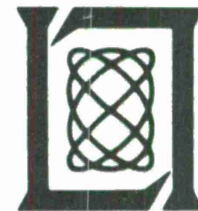
1977

Prepared  
under Electronic Systems Division Contract F19628-76-C-0002 by

**Lincoln Laboratory**

MASSACHUSETTS INSTITUTE OF TECHNOLOGY

LEXINGTON, MASSACHUSETTS



Approved for public release; distribution unlimited.

ADP041226

The work reported in this document was performed at Lincoln Laboratory, a center for research operated by Massachusetts Institute of Technology, with the support of the Department of the Air Force under Contract F19628-76-C-0002.

This report may be reproduced to satisfy needs of U.S. Government agencies.

The views and conclusions contained in this document are those of the contractor and should not be interpreted as necessarily representing the official policies, either expressed or implied, of the United States Government.

This technical report has been reviewed and is approved for publication.

FOR THE COMMANDER

  
Raymond L. Loiselle, Lt. Col., USAF  
Chief, ESD Lincoln Laboratory Project Office

Non-Lincoln Recipients

**PLEASE DO NOT RETURN**

Permission is given to destroy this document  
when it is no longer needed.

MASSACHUSETTS INSTITUTE OF TECHNOLOGY  
LINCOLN LABORATORY

SOLID STATE RESEARCH

QUARTERLY TECHNICAL SUMMARY REPORT

1 NOVEMBER 1976 - 31 JANUARY 1977

ISSUED 29 APRIL 1977

Approved for public release; distribution unlimited.

LEXINGTON

MASSACHUSETTS



## ABSTRACT

This report covers in detail the solid state research work of the Solid State Division at Lincoln Laboratory for the period 1 November 1976 through 31 January 1977. The topics covered are Solid State Device Research, Quantum Electronics, Materials Research, Microelectronics, and Surface-Wave Technology. Funding is primarily provided by the Air Force, with additional support provided by the Army, ARPA, NSF, and ERDA.

## CONTENTS

Abstract	iii
Introduction	v
Reports on Solid State Research	viii
Organization	xii
 I. SOLID STATE DEVICE RESEARCH	 1
A. High-Sensitivity Heterodyne Radiometer Using a Tunable Diode Laser Local Oscillator	1
B. CW Operation of Distributed Feedback $\text{Pb}_{1-x}\text{Sn}_x\text{Te}$ Lasers	4
II. QUANTUM ELECTRONICS	9
A. Line-Tunable, Optically Pumped 16- $\mu\text{m}$ $\text{CO}_2$ Laser	9
B. Vibrational Energy Transfer in Simple Cryogenic Liquids	10
C. Multiphoton Absorption Processes in Polyatomic Molecules	14
III. MATERIALS RESEARCH	19
A. Zirconia Membranes for High-Temperature Electrolysis Cells	19
B. Surface States on $\text{SrTiO}_3$	21
C. X-Ray Photoemission Study of Sn-Doped Indium Oxide Films	23
IV. MICROELECTRONICS	29
A. Charge-Coupled Devices (CCDs): Programmable Transversal Filter	29
B. Charge-Coupled Devices: Imagers	31
C. Surface-Oriented GaAs Schottky-Barrier Diodes	32
D. Double-Reticle Method of Eliminating Repeated Defects in Masks	35
V. SURFACE-WAVE TECHNOLOGY	39
A. Bismuth Germanium Oxide (BGO) Reflective-Array Compressors	39

## INTRODUCTION

### I. SOLID STATE DEVICE RESEARCH

By using a commercial PbSnSe diode laser operated in a cryogenic closed-cycle cooler and a state-of-the-art HgCdTe photodiode, high-resolution absorption spectra of ethylene were obtained by heterodyne radiometry. The observed signal-to-noise ratio obtained with the diode laser LO and a blackbody source was only about a factor of 2 less than the best S/N obtained using a CO<sub>2</sub> laser LO. The latter was about 45 percent of the theoretical limit for an ideal heterodyne receiver. The diode laser driven by a moderately regulated power supply was found to have a 100-kHz instantaneous linewidth.

CW operation has been achieved in distributed-feedback PbSnTe stripe-geometry double-heterostructure diode lasers grown by molecular-beam epitaxy. The lasers emit near  $\lambda \approx 12.5 \mu\text{m}$  for heat-sink temperatures between 12 and 50 K, and single-mode operation is obtained for large variations in diode current and heat-sink temperature. Also, continuous current-tuning of the mode frequency over a 7-cm<sup>-1</sup>-wide band is observed.

### II. QUANTUM ELECTRONICS

Grating tuning of the output of the HBr-pumped 16- $\mu\text{m}$  CO<sub>2</sub> laser has been accomplished. With the tuned cavity, experiments elucidating the kinetics of this laser medium have been performed. In addition, 1/3 mJ of energy in a single pulse was obtained.

Studies of the vibrational kinetics of simple liquids have been extended with the investigation of CH<sub>3</sub>F and SF<sub>6</sub> kinetics in liquid Ar and O<sub>2</sub> hosts by means of saturation techniques. For CH<sub>3</sub>F, a simple saturation behavior with a  $150 \pm 50$ -nsec V-T decay time was found. SF<sub>6</sub> exhibits a more complex behavior due to excited-state absorption processes: rate limiting steps of  $54 \pm 15$  psec in liquid O<sub>2</sub>, and  $320 \pm 80$  psec in liquid Ar were found. The implications of the molecular spectroscopy in the cryogenic liquid environment for the modeling of vibrational energy flow within these molecules have been considered.

Acoustic spectrophone measurements of the absorption of pulsed CO<sub>2</sub> laser radiation by cooled and room-temperature SF<sub>6</sub> have been made in order to study multi-photon absorption processes in polyatomic molecules. The absorption shows a strong dependence on laser frequency, laser energy, and temperature.

### III. MATERIALS RESEARCH

A technique has been developed for the fabrication of thin, corrugated, stabilized-zirconia disks that could be used as membranes for oxygen-ion transport in high-temperature electrolysis cells. A slurry of zirconia in an organic solvent is

spread on a glass plate to form a rubbery "green sheet," which is then deformed to the desired shape, fired at 1600°C in air, and finally fired at 2200°C in a reducing atmosphere to give a high-density, translucent ceramic.

The role of semiconductor surface states in the photoelectrolysis of water is being investigated by means of in situ photoresponse measurements on  $\text{SrTiO}_3$  electrodes in photoelectrochemical cells. Photons with below-bandgap energies excite photocurrents with long time constants (of the order of minutes) that are associated with the reduction of  $\text{O}_2$  by electrons transferred from the surface states of  $\text{SrTiO}_3$  to the conduction band.

Thin films of Sn-doped  $\text{In}_2\text{O}_3$ , which can be used as heat mirrors for solar collectors and as transparent electrodes for solar cells, have been studied by x-ray photoemission spectroscopy in an attempt to understand the factors determining their electrical and optical properties. The photoemission data suggest that darkening of such films, which seriously reduces their usefulness, is due to formation of an  $\text{Sn}_3\text{O}_4$ -like second phase.

#### IV. MICROELECTRONICS

A chip has been designed to add n-channel MOS shift registers and latch circuits to the original prototype CCD programmable transversal filter structure. In the prototype device, the tap weights were programmable as digital words which were controlled by switches external to the chip, but in the final device the digital words are to be stored on the chip in static logic devices. The analog input structure to the CCD sections has also been modified to make it controllable by the positive voltage levels of the logic devices.

Electrical characterization of the first of the 100- × 400-cell CCD imaging devices to be fabricated for the GEODSS (Ground Electro-Optical Deep Space Surveillance) program has begun. The time constants and densities of two trap levels thought to be responsible for transfer inefficiency have been identified by using a technique based on sequentially injected electrical signals. The most prominent source of transfer loss is a trap level which appears to be the acceptor level of gold located near the middle of the band gap.

Small, planar, surface-oriented Schottky diodes in which both terminals of the rectifying junction are on the same surface of the GaAs wafer have been fabricated and operated for the first time as detectors at submillimeter wavelengths. The planar configuration lends itself naturally to an integrated circuit approach, enabling the connection of matched strip-line antennas and IF filter networks. Diodes with diameters as small as 2  $\mu\text{m}$  have been fabricated and evaluated as harmonic mixers up to 668 GHz.

Quantitative measurements have been made of photoresist linewidth as a function of exposure time and exposure order for the double-reticle technique used to eliminate faults, which arise from particulate contamination or emulsion defects in the 10X reticle, in chromium-coated master masks. In this technique, the mask is



exposed in the step-and-repeat camera with a reticle having nominal-sized geometries and with a second reticle having slightly oversized geometries. These measurements indicate that the exposure time per reticle to achieve a desired linewidth is less for the double-reticle technique than when using a single reticle, and that exposing the oversized reticle first in the double-reticle process results in longer total exposure times for optimum linewidths.

## V. SURFACE-WAVE TECHNOLOGY

The program to develop surface-acoustic-wave (SAW) pulse expanders and compressors for the MASR (Multiple-Antenna Surveillance Radar) system has been completed. The devices were fabricated in the reflective-array-compressor (RAC) configuration on bismuth germanium oxide (BGO). Sets of devices were developed to generate and process a narrowband linear-FM waveform (2.5 MHz, 125  $\mu$ sec) and a wideband waveform (10 MHz, 150  $\mu$ sec). The low surface-wave velocity on BGO allowed compact devices capable of processing these relatively large dispersions to be fabricated on commercially available 15-cm substrates. Low spurious levels, large dynamic range, large compression ratios, and good sidelobe suppression are characteristic features of these devices. Good control of phase and amplitude response yields peak near-in sidelobes of 35 dB, and the unique RAC geometry suppresses far-out sidelobes by more than 80 dB.

# REPORTS ON SOLID STATE RESEARCH

15 November 1976 through 15 February 1977

## PUBLISHED REPORTS

### Journal Articles

#### JA No.

4591	Doppler-Limited and Atmospheric Spectra of the 4- $\mu$ m $\nu_1 + \nu_3$ Combination Band of SO <sub>2</sub>	A. S. Pine P. F. Moulton	J. Mol. Spectrosc. <u>64</u> , 15 (1977)
4611	Laser-Induced Surface Damage of Infrared Nonlinear Materials	H. Kildal G. W. Iseler	Appl. Opt. <u>15</u> , 3062 (1976)
4637	Phenomenological Theory of Raman Scattering in Europium Chalcogenides	S. A. Safran* B. Lax* G. Dresselhaus	Solid State Commun. <u>19</u> , 1217 (1976)
4651	Fluorescence and Dissociative Energy Transfer in High Pressure Ar-HCN Mixtures Excited by Relativistic Electrons	E. Zamir* A. Szöke* R. Osgood	J. Chem. Phys. <u>65</u> , 4885 (1976)
4661	Relaxation Oscillations in Distributed Feedback Lasers	S. R. Chinn	Opt. Commun. <u>19</u> , 208 (1976)
4663	Optical Phonons in AgGaSe <sub>2</sub>	A. Miller* G. D. Holah* W. D. Dunnett* G. W. Iseler	Phys. Status Solidi B <u>78</u> , 569 (1976)
4681	Preparation and Properties of PbS Crystals with Low Carrier Concentrations	T. C. Harman A. J. Strauss	J. Electron. Mater. <u>5</u> , 621 (1976)

### Meeting Speeches

#### MS No.

3986	Planar HgCdTe Quadrantal Heterodyne Arrays with GHz Response at 10.6 $\mu$ m	D. L. Spears	Infrared Phys. <u>17</u> , 5 (1977)
4045A	Electron Energy Loss Spectroscopy of Surface States on Titanium and Vanadium Oxides	V. E. Henrich H. J. Zeiger G. Dresselhaus	Proc. Workshop on Electrocatalysis of Non-Metallic Surfaces, Bethesda, Maryland, 9-12 December 1975, p. 133

\* Author not at Lincoln Laboratory.

MS No.

- |       |   |   |  |
|-------|---|---|--|
| 4067G | Scalable Tunable IR Lasers                                  | A. Mooradian  | In <u>Tunable Lasers and Applications</u> , edited by A. Mooradian, T. Jaeger, and P. Stokseth (Springer-Verlag, Berlin, 1976), p. 60  |
| 4140  | Photoelectrolysis of Water                                  | J. G. Mavroides<br>D. I. Tchernev<br>J. A. Kafalas<br>D. F. Kolesar | Proc. Workshop on Electrocatalysis of Non-Metallic Surfaces, Bethesda, Maryland, 9-12 December 1975, p. 221                            |
| 4143  | Stark Model of the Excitonic Surface States Observed on MgO | H. J. Zeiger<br>V. E. Henrich<br>G. Dresselhaus                     | Proc. Workshop on Electrocatalysis of Non-Metallic Surfaces, Bethesda, Maryland, 9-12 December 1975, p. 59                             |
| 4174A | Optically Pumped Gas Lasers                                 | H. Kildal<br>T. F. Deutsch  | In <u>Tunable Lasers and Applications</u> , edited by A. Mooradian, T. Jaeger, and P. Stokseth (Springer-Verlag, Berlin, 1976), p. 367 |
| 4319  | Convolvers for DPSK Demodulation of Spread Spectrum Signals | S. A. Reible<br>J. H. Cafarella<br>R. W. Ralston<br>E. Stern        | In <u>1976 Ultrasonics Symposium Proceedings</u> (IEEE, New York, 1976), p. 451  |
| 4320  | A Continuously Variable Delay-Line System                   | V. S. Dolat<br>R. C. Williamson                                     | In <u>1976 Ultrasonics Symposium Proceedings</u> (IEEE, New York, 1976), p. 419  |
| 4332  | Lincoln Laboratory Program on Thin-Film Photovoltaics       | H. J. Zeiger  | Proc. ERDA Solar Photovoltaic Program Review Meeting, University of Maine, Orono, 3-5 August 1976, p. 908                              |

\* \* \* \* \*

## UNPUBLISHED REPORTS

Journal ArticlesJA No.

- |      |   |  |                                       |
|------|---|--|---------------------------------------|
| 4622 | Infrared Third-Harmonic Generation in Phasematched CO Gas                   | H. Kildal  | Accepted by IEEE J. Quantum Electron. |
| 4629 | Graphite Intercalation Compounds; Electronic Properties in the Dilute Limit | M. S. Dresselhaus*<br>G. Dresselhaus<br>J. E. Fischer* | Accepted by Phys. Rev. B              |
| 4666 | Temperature-Gradient LPE Growth of $Pb_{1-x}Sn_xTe$                         | S. H. Groves   | Accepted by J. Electron. Mater.       |

---

\* Author not at Lincoln Laboratory.

JA No.

4677	Submillimeter Heterodyne Detection with Planar GaAs Schottky Barrier Diodes	R. A. Murphy C. O. Bozler C. D. Parker H. R. Fetterman P. E. Tannenwald B. J. Clifton J. P. Donnelly W. T. Lindley	Accepted by IEEE Trans. Microwave Theory Tech.
4684	Microscopic Theory of the Lattice Dynamics of HCP Rare-Earth Metals	J. C. Upadhyaya* A. O. E. Animalu	Accepted by Phys. Rev. B
4693	Resonant Infrared Third-Harmonic Generation in Cryogenic Liquids	H. Kildal S. R. J. Brueck	Accepted by Phys. Rev. Lett.
4700	Low-Dose n-Type Ion Implantation into Cr-Doped GaAs Substrates	J. P. Donnelly C. O. Bozler W. T. Lindley	Accepted by Solid-State Electron.
4703	1500-Hour Continuous CW Operation of Double-Heterostructure GaInAsP/InP Lasers	C. C. Shen J. J. Hsieh T. A. Lind	Accepted by Appl. Phys. Lett.
4708	Schottky Barrier Diodes for Submillimeter Heterodyne Detection	B. J. Clifton	Accepted by IEEE Trans. Microwave Theory Tech.
MS-4230A	$\text{In}_x\text{Ga}_{1-x}\text{As}_y\text{P}_{1-y}/\text{InP}$ Double-Heterostructure Lasers	J. A. Rossi J. J. Hsieh J. P. Donnelly	Accepted for Proc. 1976 North American Symposium on Gallium Arsenide and Related Compounds, St. Louis, 26-29 September 1976
MS-4271	X-Ray Lithography	H. I. Smith D. C. Flanders	Accepted by Jap. J. Appl. Phys.
MS-4302	Ion Implantation in GaAs	J. P. Donnelly	Accepted for Proc. 1976 North American Symposium on Gallium Arsenide and Related Compounds, St. Louis, 26-29 September 1976

Meeting Speeches†

MS No.

4140E	Photoelectrolysis of Water	J. G. Mavroides	Boston College Physics Colloquium, Boston, 9 February 1977
4230D	Double-Heterostructure GaInAsP/InP Diode Lasers	J. J. Hsieh	Honeywell Corporate Research Center, Bloomington, Minnesota, 7 December 1976

\* Author not at Lincoln Laboratory.

† Titles of Meeting Speeches are listed for information only. No copies are available for distribution.

MS No.

4309A	High-Temperature Electrolysis and Fuel Cells	T. B. Reed	Energy Seminar, Brookhaven National Laboratory, Upton, New York, 30 November 1976
4335	Schottky Barrier Diodes for Submillimeter Heterodyne Detection	B. J. Clifton	Second International Conference and Winter School on Submillimeter Waves and Their Applications, San Juan, Puerto Rico, 6-10 December 1976
4337	Internal Cavity, Optically Pumped Molecular Laser	H. R. Fetterman H. R. Schlossberg*	
4388	Submillimeter Heterodyne Detection Using Surface-Oriented Schottky Diodes	R. A. Murphy C. O. Bozler C. D. Parker H. R. Fetterman B. J. Clifton J. P. Donnelly W. T. Lindley P. E. Tannenwald	
4343	Second and Fourth Order Nonlinear Processes in Chalcopyrites	H. Kildal G. W. Iseler N. Menyuk J. C. Mikkelsen*	Topical Meeting on Optical Phenomena in Infrared Materials, Annapolis, Maryland, 1-3 December 1976
4358	Semiconductor-Based Infrared Integrated Optics	I. Melngailis	
4344	Molecular-Beam Epitaxy in the Lead-Tin Chalcogenides	J. N. Walpole	Annual Meeting of Materials Research Society, Cambridge, Massachusetts, 15-17 November 1976
4362	Studies of Defect Surface States on SrTiO <sub>3</sub> Photoelectrolytic Electrodes	J. G. Mavroides V. E. Henrich H. J. Zeiger G. Dresselhaus J. A. Kafalas D. F. Kolesar	
4381	Adsorption of O <sub>2</sub> and H <sub>2</sub> O by Surface Defects on TiO <sub>2</sub> and SrTiO <sub>3</sub>	V. E. Henrich G. Dresselhaus H. J. Zeiger	Workshop on Physical Adsorption, Brookhaven National Laboratory, Upton, New York, 28-30 December 1976

---

\* Author not at Lincoln Laboratory.

## ORGANIZATION

### SOLID STATE DIVISION

A. L. McWhorter, *Head*  
 I. Melngailis, *Associate Head*  
 C. R. Grant, *Assistant*  
 P. E. Tannenwald

#### QUANTUM ELECTRONICS

A. Mooradian, *Leader*  
 P. L. Kelley, *Associate Leader*

Barch, W. E.	Heckscher, H.
Brueck, S. R. J.	Kildal, H.
Burke, J. W.	Larsen, D. M.
Chinn, S. R.	Menyuk, N.
DeFeo, W. E.	Moulton, P. F.
Deutsch, T. F.	Osgood, R. M.
Fetterman, H. R.	Parker, C. D.
Flemming, M. W.*	Pine, A. S.
Hancock, R. C.	

#### ELECTRONIC MATERIALS

A. J. Strauss, *Leader*  
 H. J. Zeiger, *Associate Leader*

Anderson, C. H., Jr.	Kolesar, D. F.
Animalu, A. O. E.	Krohn, L., Jr.
Button, M. J.	LaFleur, W. J.
Delaney, E. J.	Mastromattei, E. L.
Dresselhaus, G.	Mavroides, J. G.
Dwight, K., Jr.	Mroczkowski, I. H.
Fahey, R. E.	Owens, E. B.
Fan, J. C. C.	Palm, B. J.
Feldman, B.	Pantano, J. V.
Finn, M. C.	Pierce, J. W.
Gay, R. R.*	Reed, T. G.
Henrich, V. E.	Spura, S.†
Hong, H. Y-P.	Tchernev, D. I.
Hsieh, J. J.	Tracy, D. M.
Iseler, G. W.	Vohl, P.
Kafalas, J. A.	

#### APPLIED PHYSICS

A. G. Foyt, *Leader*  
 T. C. Harman, *Assistant Leader*  
 C. E. Hurwitz, *Assistant Leader*

Belanger, L. J.	Lind, T. A.
Calawa, A. R.	McBride, W. F.
Carter, F. B.	Paladino, A. E.
DeMeo, N. L., Jr.	Plonko, M. C.
Donnelly, J. P.	Shen, C. C.
Ferrante, G. A.	Spears, D. L.
Groves, S. H.	Tsang, D.*
Leonberger, F. J.	Walpole, J. N.

#### SURFACE WAVE TECHNOLOGY

E. Stern, *Leader*  
 R. C. Williamson, *Assistant Leader*

Baker, R. P.	Kernan, W. C.
Brogan, W. T.	Li, R. C. M.
Cafarella, J. H.	Melngailis, J.
DeGraff, P. D.	Ralston, R. W.
Dolat, V. S.	Reible, S. A.
Efremow, N., Jr.	Smith, H. I.
Flanders, D. C.*	Viannes, N.*
Hurlburt, D. H.	

#### MICROELECTRONICS

W. T. Lindley, *Leader*  
 F. J. Bachner, *Assistant Leader*

Beatrice, P. A.	Gray, R. V.
Bozler, C. O.	Hansell, G. L.*
Burke, B. E.	Lincoln, G. A., Jr.
Chiang, A. M.	McGonagle, W. H.
Clifton, B. J.	Mountain, R. W.
Clough, T. F.	Murphy, R. A.
Cohen, R. A.	Pichler, H. H.
Daniels, P. J.	Silversmith, D. J.
Durant, G. L.	Smythe, D. L.
Foley, G. H.	Wilde, R. E.
Grant, L. L.	

\* Research assistant

† Co-op. student

## I. SOLID STATE DEVICE RESEARCH

### A. HIGH-SENSITIVITY HETERODYNE RADIOMETER USING A TUNABLE DIODE LASER LOCAL OSCILLATOR

Active laser techniques based on scattering, fluorescence, and resonant absorption have been successfully applied to the detection of atmospheric constituents. Field monitoring instruments and systems have also been developed for continuous ambient air study.<sup>1</sup> Recently, laser heterodyne radiometry has been advocated as a completely passive method to detect gas absorption and emission lines, and infrared heterodyne systems with CO<sub>2</sub> and CO gas laser local oscillators have been used for pollutant measurements<sup>2</sup> as well as for astronomical purposes.<sup>3</sup> However, the usefulness of these gas laser systems is limited by a dependence upon an accidental coincidence of laser frequency with the characteristic gas line. Heterodyne systems would be much more versatile if a broadly tunable laser, such as a diode laser, could be used for the local oscillator (LO). Here we report high-resolution spectroscopy of C<sub>2</sub>H<sub>4</sub> obtained with a diode-laser heterodyne system which has shown a sensitivity over an order of magnitude greater than previously<sup>4</sup> obtained with diode lasers, and within a factor of 2 of the quantum-noise-limited sensitivity we achieved with a CO<sub>2</sub> laser LO.

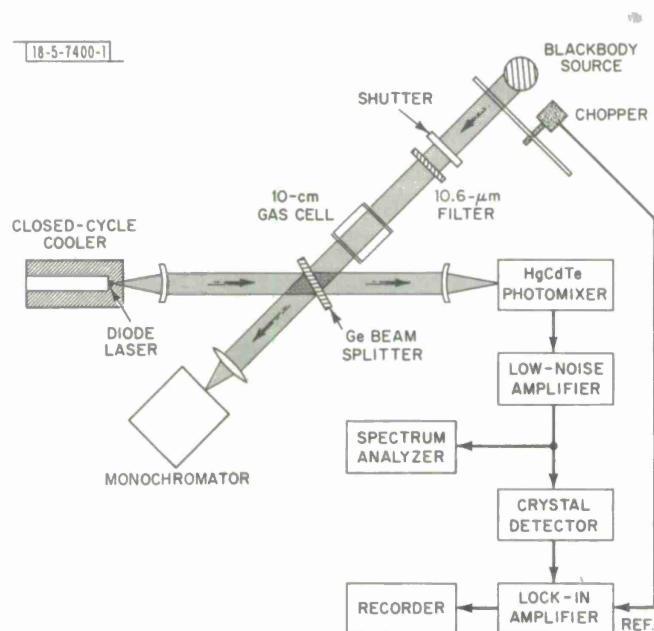


Fig. I-1. Experimental setup used for diode laser heterodyne radiometry.

Figure I-1 shows schematically the heterodyne setup which utilizes a 900°C blackbody source and a tunable 10.6-μm PbSnSe diode laser<sup>†</sup> LO mounted in a closed-cycle cooler. The diode laser was at about 30 K for the heterodyne measurements. The LO wavelength was coarse-tuned by adjusting the cooler temperature, and fine-tuned by adjusting the laser current. This laser radiation was combined with the thermal emission at the beam splitter and focused onto a

<sup>†</sup> We are grateful to Laser Analytics, Inc. for providing the diode laser for this work.



state-of-the-art HgCdTe photodiode,<sup>5</sup> which has a bandwidth of over 1.5 GHz and an effective heterodyne quantum efficiency<sup>6</sup>  $\eta_e$  of 0.4. The photodiode was mounted in a liquid-nitrogen dewar. A spectrum analyzer was used to monitor the IF noise.

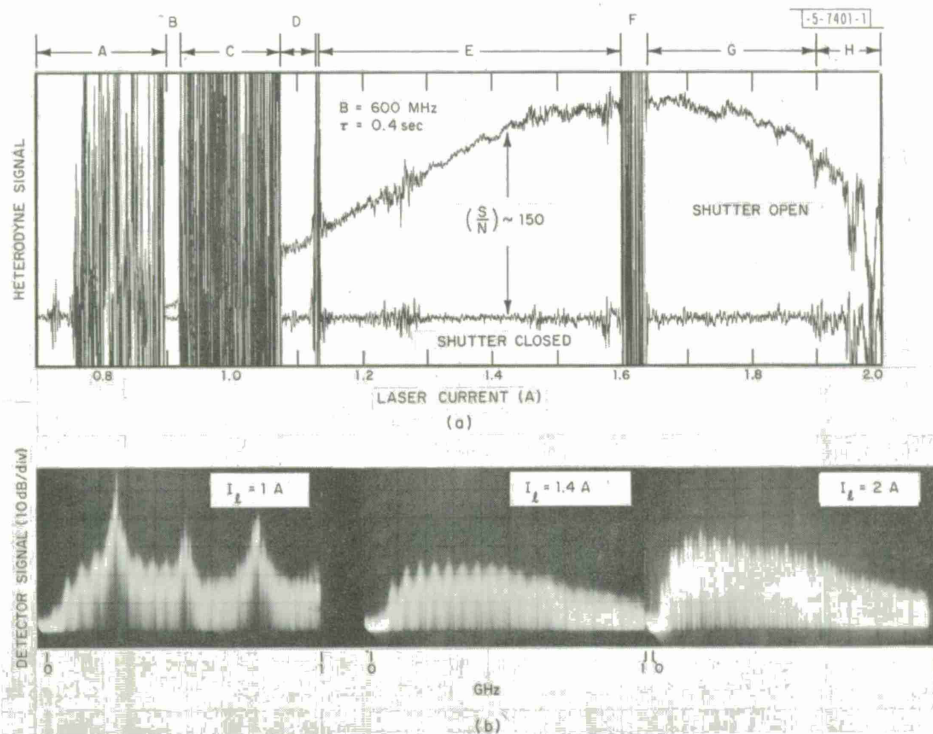


Fig. I-2. (a) Heterodyne signal as a function of diode laser LO current (i.e., wavelength). Amplifier noise level was somewhat less than lowest level observed with LO on, as shown at 1.4 A, with shutter closed. (b) Preamplifier RF noise spectra in 0- to 1-GHz region for three different laser currents showing LO noise (noise bandwidth = 100 kHz).

Heterodyne signal-to-noise ( $S/N$ ) was found to be largely dependent upon properties of the diode laser LO, such as the power available at the photomixer and excess RF noise generated by the diode laser. A typical scan of the heterodyne signal as a function of diode laser current is shown in Fig. I-2(a) for a diode laser with three or four dominant modes in the  $\sim 20\text{-cm}^{-1}$  (600-GHz) scan range. Note the occurrence of several very noisy regions (A, C, F, H) which are unsuitable for heterodyne detection and appear to be associated with mode switching and self-beating of laser modes. IF noise spectra in the 0- to 1-GHz region shown in Fig. I-2(b) reveal quite different noise output in regions C and H as compared with that of region E, where the LO was relatively well-behaved. In region C, strong self-beat signals were detected, and in region H an excessively high "white" noise spectrum was seen. Vibration of the diode on the cooler cold head probably contributed in part to this noisy performance; however, the phenomenon is a general property of diode lasers, as we have seen similar effects with diodes mounted in a liquid-helium dewar. Nevertheless, the best  $S/N$  ( $S/N = 150$ ) found at  $I = 1.42$  A in Fig. I-2(a) is only about a factor of 6 less than  $S/N \approx 900$  calculated for an ideal ( $\eta_e = 1$ )  $10.6\text{-}\mu\text{m}$  radiometer from the expression

$$S/N = 2\eta_e (Br)^{1/2} T_o (\exp[h\nu/kT - 1])^{-1}$$



and using our experimental parameters  $T = 1173$  K,  $B = 500$  MHz, and  $\tau = 0.4$  sec. A total transmission factor  $T_0$  of 0.077 was due principally to the beam splitter, filter, and chopper factors of 0.36, 0.62, and 0.50, respectively. This observed S/N is substantially better than that generally reported for systems using  $\text{CO}_2$  laser LOs, which is probably due to the higher  $\eta_e$  (0.4) of our HgCdTe photodiode. This result is very encouraging since it was obtained with only 0.15 mW of LO power on the photodiode, and compares favorably with the quantum-noise-limited S/N value of 290 we obtained with a 0.4-mW  $\text{CO}_2$  laser LO.

The linewidth of one of the diode laser modes was measured by mixing the laser mode with the  $\text{CO}_2$  P(20) line. A 100-kHz instantaneous linewidth was observed using a moderately regulated power supply. This compares favorably with the 54-kHz linewidth of previous measurements<sup>7</sup> on a single-mode PbSnTe diode laser with comparable output power. The measurements in Ref. 7 were carried out using a diode mounted in a liquid-helium heat-sink dewar in conjunction with a highly stable power supply.

Ethylene spectroscopy was performed by first placing a 10-cm gas cell in the diode laser beam and directly measuring the absorption to locate the  $\text{C}_2\text{H}_4$  lines. Figure I-3(a) shows the transmission signal as a function of diode laser current, where the dominant laser mode was tuned through several  $\text{C}_2\text{H}_4$  lines near  $942\text{ cm}^{-1}$ . Line position and laser tuning rate were established by heterodyne calibration with the P(22) line of a stabilized  $\text{CO}_2$  laser. Figure I-3(b)

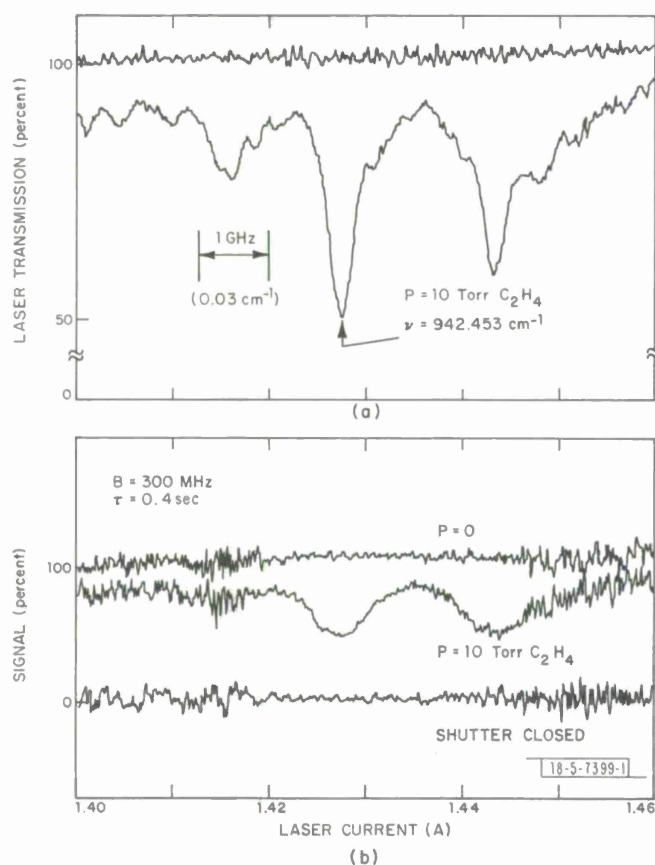


Fig. I-3. (a) Direct diode laser absorption scan of three  $\text{C}_2\text{H}_4$  lines near  $942\text{ cm}^{-1}$ . (b) Heterodyne absorption scan of above lines with spectral resolution of  $2B = 600$  MHz ( $0.02\text{ cm}^{-1}$ ).

displays the line spectra obtained by tuning the diode laser LO over the same range in a heterodyne absorption experiment where the  $C_2H_4$  cell was placed in front of the blackbody source. The line profile is in good agreement with the IF resolution of 600 MHz ( $0.02\text{ cm}^{-1}$ ). With a slightly improved diode laser LO, we expect to achieve twice this sensitivity for use in passive monitoring of gas absorption and emission lines in the atmosphere and stratosphere.

R. T. Ku (Group 51)  
D. L. Spears

## B. CW OPERATION OF DISTRIBUTED FEEDBACK $Pb_{1-x}Sn_xTe$ LASERS

We previously reported<sup>8</sup> pulsed operation of distributed feedback (DFB) injection lasers in  $Pb_{1-x}Sn_xTe$  double heterostructures (DHs) grown by molecular-beam epitaxy. Here we report CW operation of similar devices operating near  $\lambda \approx 12.5\text{ }\mu\text{m}$  wavelength for heat-sink temperatures between 12 and 50 K. Single-mode operation is obtained for large variations in diode current and heat-sink temperature. Also, continuous current tuning of the mode frequency up to  $\approx 7\text{ cm}^{-1}$  is observed. These performance features of the DFB structure, as opposed to Fabry-Perot (FP) devices, offer significant advantages in tunable laser spectroscopy<sup>9</sup> and in applications as tunable LOs.<sup>9,10</sup>

As in the previous pulsed DFB lasers,<sup>8</sup> the grating of  $1.1\text{-}\mu\text{m}$  periodicity operates in the first Bragg order and was etched into the surface of the top DH layer<sup>11</sup> after all epitaxy had been completed. Striped mesas  $32\text{ }\mu\text{m}$  wide were formed and the devices were fabricated as described in Ref. 8 (except as noted below), so that the lasers have electrically active regions  $450\text{ }\mu\text{m}$  in length at the output end of the mesas and electrically insulated regions of comparable length at the other end to spoil the FP cavity. For comparison, one device was fabricated with the inactive length cleaved off so that both distributed feedback as well as reflective feedback from each end of the cavity could be obtained.

In addition to the fabrication procedures described in Ref. 8, the following processes were used. After the sputter-etching of the grating and of the striped mesas, and after removal of all photoresist by plasma oxidation, the wafer was again sputter-etched in Ar at low voltage to remove approximately  $50\text{ }\text{\AA}$  from the surface. Then the wafer was placed in flowing  $H_2$  and heated to  $425^\circ\text{C}$  for 10 min. These additional steps were taken in an attempt to eliminate a possibly oxidized and/or damaged layer resulting from the sputter-etching and plasma oxidation. The current-voltage characteristics of the resulting devices were improved over those of Ref. 8. Less leakage current was observed near zero bias, and forward-limiting resistances were in the range  $0.06$  to  $0.1\text{ }\Omega$ . Threshold current densities were reduced from  $\sim 19\text{ kA/cm}^2$  to values in the range of  $3$  to  $6\text{ kA/cm}^2$ , and CW operation was achieved up to  $\sim 22\text{ kA/cm}^2$ .

The tuning characteristics (mode frequencies in  $\text{cm}^{-1}$  vs diode current) at 12 and 25 K for one of the devices are shown in Fig. I-4. At 12 K, there are two modes with unusual tuning characteristics. The lowest threshold mode disappears at about 2.6 A, and a second mode at lower energy appears. (In  $PbSnTe$  FP lasers, as the current increases, modes typically appear at higher energies since the spontaneous line shifts in that direction.) Finally, as shown by the dashed extrapolation, the original mode returns at about 3.3 A. This type of behavior may be related to simultaneous DFB operation and some residual independent reflective feedback from the unpumped region.<sup>12</sup> At 25-K heat-sink temperature, two additional modes appear at considerably higher frequencies. This particular device was operated up to 45 K where two more

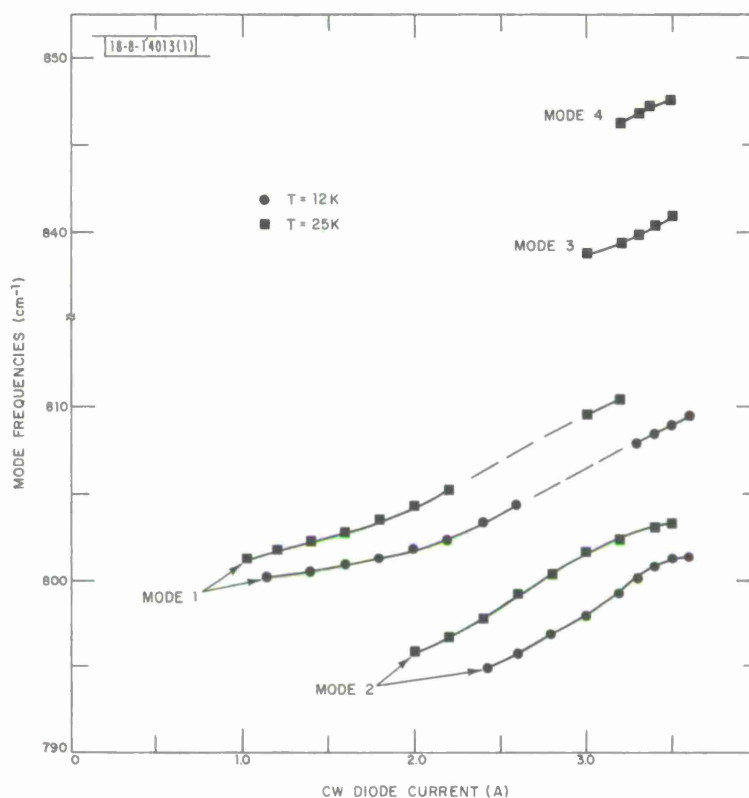


Fig. I-4. Mode frequencies of a PbSnTe DFB diode laser plotted vs CW diode current for heat-sink temperatures of 12 and 25 K. Modes labeled 1 and 2 tune continuously with heat-sink temperature between curves shown. Gap in tuning characteristics of mode 1 is indicated by dashed lines. Modes 3 and 4 are not present at 12 K.

modes at higher frequencies were observed at the higher currents. The two lowest threshold modes shown in Fig. I-4 were present at all temperatures. The origin of the various modes has not been determined. They may result from higher-order transverse modes in the plane of the junction, as well as from reflective feedback effects mentioned above.<sup>12</sup>

As the energy gap of the PbSnTe increases with temperature, the possible emission range of the device no longer coincides with the grating period, and DFB operation ceases. For the device in Fig. I-4 this occurs near 45 K, above which the laser emission rapidly becomes weak. This temperature varies slightly with variations in device heat-sinking, and other devices showed DFB operation up to ~50 K. In comparison, the device in which the inactive length had been cleaved off to obtain both distributed feedback and strong reflective feedback showed behavior more typical of FP devices. Ten or more modes could be seen simultaneously, and CW operation persisted up to ~80 K. The modes, however, had an unusually large, irregular spacing with long continuous tuning ranges up to 4 cm<sup>-1</sup>, rather than the 1 to 2 cm<sup>-1</sup> typically seen in pure FP devices.<sup>9</sup> In Fig. I-5, this device (labeled FP + DFB) is compared with the DFB device discussed above. The observed mode frequencies for currents of 2 A are plotted vs heat-sink temperature.

Figure I-6 shows the frequencies in the two lowest threshold modes of the DFB laser vs diode current with heat-sink temperature as a parameter varying from 12 to 45 K. Here it can be seen that the minimum threshold occurs at ~35 K. We also note that because of the overlap

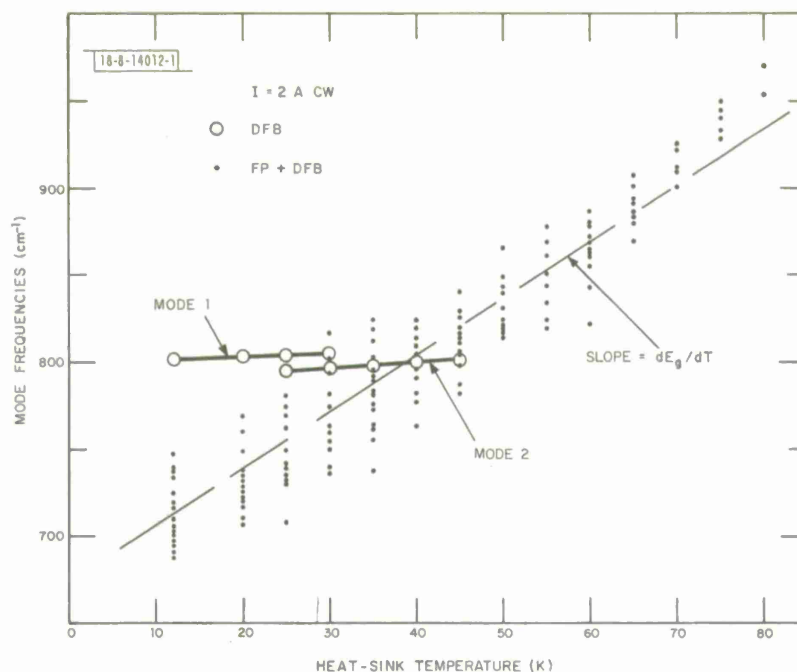


Fig.I-5. Mode frequencies of a PbSnTe DFB diode laser at 2 A compared with mode frequencies of device having both DFB and reflective feedback (labeled FP + DFB) as a function of heat-sink temperature. Dashed line with slope labeled  $dE_g/dT$  shows temperature dependence of spontaneous emission. At 2 A, only modes 1 and 2 are seen at any temperature for DFB laser.

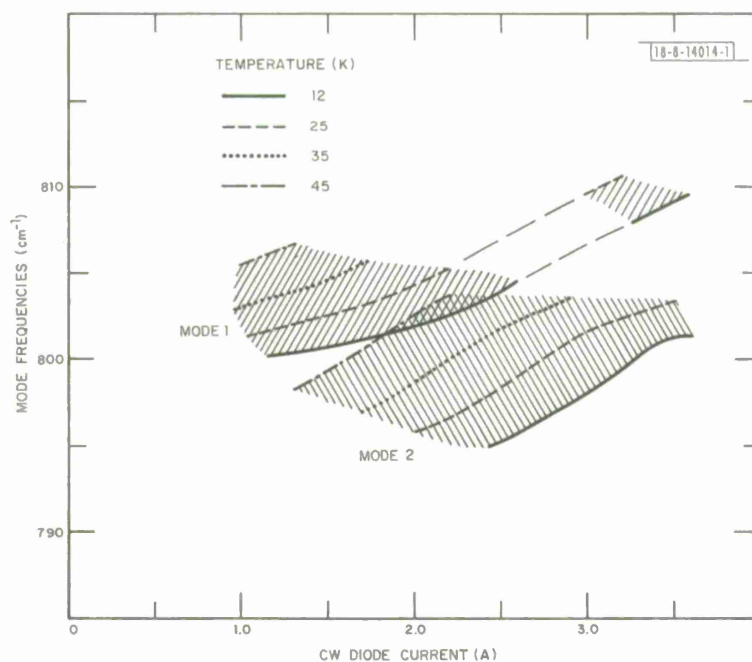


Fig.I-6. Frequencies of two lowest threshold modes of a PbSnTe DFB laser vs diode current with heat-sink temperature varying as indicated between 12 and 45 K. Two-parameter (current-temperature) tuning range of mode 1 consists of two regions with gap in emission indicated by dashed lines.

in frequencies of the two modes, with two-parameter tuning, a continuous tuning range (i.e., without a gap) of over  $11 \text{ cm}^{-1}$  can be achieved in this case.

At present, these devices are comparable in threshold current density and output power (up to  $100 \text{ } \mu\text{W}$  from one end) to similar FP devices reported earlier<sup>13</sup> which operated CW up to 114 K. By comparison with the emission wavelengths of these FP devices, we conclude that CW operation of DFB devices above 77 K operating in the wavelength range of  $8.5$  to  $12 \text{ } \mu\text{m}$  is now feasible with proper choice of grating periodicity.

J. N. Walpole    S. H. Groves  
A. R. Calawa    T. C. Harman  
S. R. Chinn

#### REFERENCES

1. Laser Monitoring of the Atmosphere, E. D. Hinkley, Editor (Springer-Verlag, New York, 1976).
2. R. T. Menzies and M. S. Shumate, *Appl. Opt.* **15**, 2080 (1976).
3. D. W. Peterson, M. A. Johnson, and A. L. Betz, *Nature* **250**, 128 (1974).
4. M. Mumma, T. Kostiuk, S. Cohen, D. Buhl, and P. C. von Thuna, *Spac. Opt. Rev.* **17**, 661 (1975).
5. D. L. Spears, I. Melngailis, and T. C. Harman, *IEEE J. Quantum Electron.* **QE-11**, 79D (1975); D. L. Spears, *Infrared Phys.* **17**, 5 (1977).
6. Solid State Research Report, Lincoln Laboratory, M.I.T. (1976:3), p. 5, DDC AD-A034647.
7. E. D. Hinkley and C. Freed, *Phys. Rev. Lett.* **23**, 277 (1969), DDC AD-694147.
8. J. N. Walpole, A. R. Calawa, S. R. Chinn, S. H. Groves, and T. C. Harman, *Appl. Phys. Lett.* **29**, 307 (1976), DDC AD-A031649.
9. E. D. Hinkley, K. W. Nill, and F. A. Blum, in Topics in Applied Physics, Laser Spectroscopy of Atoms and Molecules, H. Walther, Editor (Springer-Verlag, Berlin, 1974), Vol. 2, p. 125.
10. E. D. Hinkley and P. L. Kelley, *Science* **171**, 635 (1971), DDC AD-723786.
11. This design for AlGaAs grating-coupled lasers was discussed earlier by P. Zory and L. D. Comerford in *IEEE J. Quantum Electron.* **QE-11**, 451 (1975).
12. As discussed in Ref. 8, the unpumped region may act as a distributed Bragg reflector with a different Bragg frequency, or simply as a region of slightly different guide index. In any case, Chinn [S. R. Chinn, *IEEE J. Quantum Electron.* **QE-9**, 574 (1973), DDC AD-771837/2] has shown that thresholds for modes involving both DFB and reflective feedback are dependent on the phase shift of the reflected component which, in the present case, will vary with current tuning of the index. Consequently, mode hopping can result from large changes in mode thresholds with current.
13. J. N. Walpole, A. R. Calawa, T. C. Harman, and S. H. Groves, *Appl. Phys. Lett.* **28**, 552 (1976), DDC AD-A027012/4.





## II. QUANTUM ELECTRONICS

### A. LINE-TUNABLE, OPTICALLY PUMPED 16- $\mu\text{m}$ CO<sub>2</sub> LASER

We have developed an optically pumped CO<sub>2</sub> laser at 16 and 14  $\mu\text{m}$  which is both "line" tunable and moderately energetic. It is, therefore, a practical source for photochemical experiments involving either of these two wavelength regions. The operating principles of the laser have been detailed previously.<sup>1</sup> Briefly, a hydrogen halide laser (typically HBr) is used to excite a low-pressure gas sample containing both the same hydrogen halide and CO<sub>2</sub>. Vibrational transfer to the CO<sub>2</sub> from the laser-excited hydrogen halide, followed by application of a stimulating (or pumping) pulse at 9.6 or 10.6  $\mu\text{m}$ , causes inversion of the relevant 16- or 14- $\mu\text{m}$  laser levels, respectively. A summary of typical operating parameters is given in Table II-1.

TABLE II-1 TYPICAL OPERATING PARAMETERS OF 16- $\mu\text{m}$ CO <sub>2</sub> LASER	
Pulse Width	0.1 to 2 $\mu\text{sec}$
Pressure	1 Torr CO <sub>2</sub> , 1 Torr HBr, 6 Torr argon
Gas-Cell Temperature	+20° to -80°C
Required CO <sub>2</sub> Stimulating Pulse Energy	10 mJ (single mode) in 100-nsec pulse
HBr Pulse Energy	20 mJ in lines in $v = 1 \rightarrow v = 0$ band

Line-by-line tuning of the 16- $\mu\text{m}$  laser was obtained with the cavity shown in Fig. II-1. Because the 9.6- $\mu\text{m}$  pulse was supplied to the cavity from an external single-line CO<sub>2</sub> laser, both the 9.6- $\mu\text{m}$  pumping transition and the 16- $\mu\text{m}$  lasing transition could be varied independently. We observed that with a single, fixed P or R branch stimulating transition, numerous 16- $\mu\text{m}$  P, Q, or R branch transitions could be tuned into oscillation. Thus, the CO<sub>2</sub> rotational manifold was completely thermalized during both the application of the stimulating pulse and the formation of the 16- $\mu\text{m}$  pulse. The laser pulse energy in the strongest 16- $\mu\text{m}$  lines was comparable to that extracted from a cavity without a grating.

By adjusting a number of laser design parameters – chiefly output coupling, mode size, sample cell length, and gas pressure – we have substantially improved the optically pumped laser energy. The best result to date, which was obtained with a 40-cm-length cell and 20 mJ of absorbed HBr laser energy, was 0.3 mJ.<sup>†</sup> Efficiency arguments, which are based on our current understanding of the laser kinetics, indicate that further improvements in the pulse energy can be expected.

Experiments with both the line-selected 16- $\mu\text{m}$  laser and a fluorescence cell containing HBr and CO<sub>2</sub> have yielded information on the gas kinetics in the optically pumped laser medium.

<sup>†</sup> This result was obtained in a cavity containing no intracavity grating. The 16- $\mu\text{m}$  laser power was approximately  $3 \times 10^3$  W.

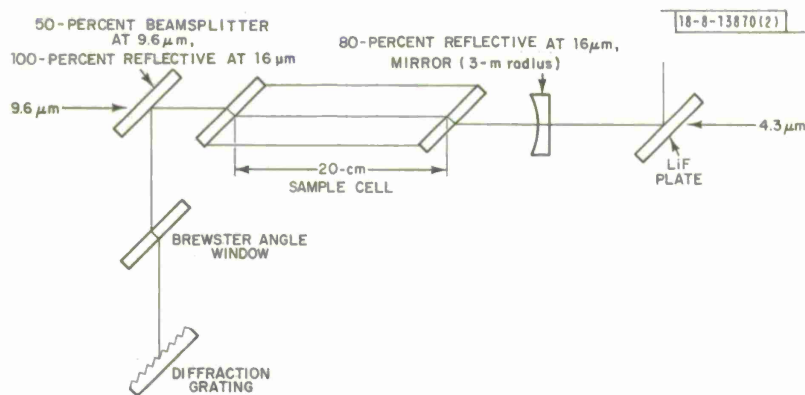


Fig. II-1. Optical cavity used for obtaining line-tuned 16- $\mu$ m laser.

Earlier measurements in the fluorescence cell showed that deactivation of the  $\text{CO}_2$   $01^{10}$  level by HBr is extremely fast, namely  $6 \times 10^4 \text{ sec}^{-1} \text{ Torr}^{-1}$ . Experiments with the line-selective cavity have shown that the rate for the deactivation of the upper 16- $\mu$ m laser level by HBr, while fast, is still slower than the rate for rotational thermalization of  $\text{CO}_2$ , i.e., approximately  $10^6 \text{ sec}^{-1} \text{ Torr}^{-1}$ .

R. M. Osgood

#### B. VIBRATIONAL ENERGY TRANSFER IN SIMPLE CRYOGENIC LIQUIDS

In a previous report<sup>2</sup> we discussed both the simplifications of the vibrational spectra of complex molecules that occur when they are dissolved in cryogenic liquid hosts such as argon, oxygen, or nitrogen, as well as some preliminary photochemistry experiments in these media. Further progress in the use of these doped cryogenic liquid systems for optically pumped laser and photochemical applications requires a detailed knowledge of vibrational energy transfer rates in these media. We have therefore undertaken a study of vibrational kinetics by investigating two molecular dopants,  $\text{CH}_3\text{F}$  and  $\text{SF}_6$ , in a variety of liquid hosts. These molecules have very different spectroscopic characteristics and exhibit varied relaxation behavior.  $\text{SF}_6$  is of current interest because in the gaseous phase it can readily be dissociated by high-intensity  $\text{CO}_2$  laser radiation;<sup>3,4</sup> however, the energy-transfer situation is only partially understood.<sup>5,6</sup> The gas-phase kinetics of  $\text{CH}_3\text{F}$  are, in contrast, rather well understood.<sup>7</sup>

Typical relaxation times in these liquid media are in the range  $10^{-9}$  to  $10^{-12}$  sec, too rapid for straightforward use of the laser-induced fluorescence techniques that have been extensively employed in gas-phase measurements.<sup>8</sup> The picosecond kinetics techniques, based mainly on nonlinear processes such as stimulated Raman scattering, which have been extensively employed for the study of neat liquids<sup>9</sup> are not applicable to these low dopant density ( $10^{16}$  to  $10^{17} \text{ cm}^{-3}$ ) liquids. We have therefore chosen to study these kinetics by measurements of the saturation of the optical absorption and by double-resonance techniques. The techniques are ideally suited to the liquid environment since the high heat capacity and thermal conductivity of the liquid eliminate spurious translational heating effects which complicate the interpretation of these experiments in low-density gaseous media. In addition, the simplified spectroscopic features of the cryogenic liquid medium allow unambiguous excitation of a single vibrational mode.

Methyl fluoride ( $\text{CH}_3\text{F}$ ) is a symmetric top molecule whose lowest energy mode,  $\nu_3$  at  $1040 \text{ cm}^{-1}$ , is accessible with  $\text{CO}_2$  laser radiation. In both liquid  $\text{O}_2$  and Ar solvents, this



nondegenerate mode has a linewidth of approximately  $4.5 \text{ cm}^{-1}$ . This linewidth is due predominantly to the hindered rotational motion of the relatively light and compact  $\text{CH}_3\text{F}$  molecule about axes perpendicular to the C-F molecular axis, and in contrast to the case of  $\text{SF}_6$  (see below) very little information regarding vibrational kinetic rates can be gleaned from this linewidth.

In the steady state, for a simple two-level system with a single relaxation time  $\tau$ , the optical transmission  $T$  is given by the expression

$$\frac{\ln(T/T_s)}{1-T} = \frac{\gamma\tau}{\hbar\omega} I_i \quad (\text{II-1})$$

where  $T_s$  is the small signal transmission,  $I_i$  is the incident intensity,  $\gamma$  is the absorption cross section, and  $\hbar\omega$  is the photon energy. A plot of the left-hand side of Eq. (II-1) vs incident intensity gives a straight line whose slope is proportional to  $\tau$ .

Saturation measurements were performed on  $\text{CH}_3\text{F}$  (and on  $\text{SF}_6$ ) in a variety of hosts by measuring the incident and transmitted  $\text{CO}_2$  TEA laser energy through a cryogenic liquid cell (5.8-cm path length) with energy meters. For  $\text{CH}_3\text{F}$ , the TEA laser was operated with an internal gain cell above CW threshold and with a gas mix that was highly  $\text{N}_2$  rich to give a 1.0- $\mu\text{sec}$ -long laser pulse with no rapid temporal structure. Figure II-2 shows the results for a  $\text{CH}_3\text{F}$  density of approximately  $1.7 \times 10^{17} \text{ cm}^{-3}$  in a liquid  $\text{O}_2$  solvent at 77 K. The measured curve is linear, and from the slope we deduce a relaxation time of  $\tau \sim 150 \pm 50 \text{ nsec}$ . This  $\tau$  is much shorter than the 1.0- $\mu\text{sec}$ -pulse width, which justifies the steady-state assumption. As expected from the very high degree of dilution, this relaxation time was independent of  $\text{CH}_3\text{F}$  concentration. An identical relaxation time, to within experimental error, was found for  $\text{CH}_3\text{F}$ -Ar solutions, in agreement with gas-phase results.<sup>7</sup> The relatively large uncertainty in the measured lifetime results from the effects of the spatial and temporal variation of the  $\text{CO}_2$  laser beam. Double-resonance experiments which involve a second CW  $\text{CO}_2$  laser operating on an adjacent transition within the vibrational bandwidth of  $\text{CH}_3\text{F}$  are currently under way and will permit a direct relaxation-time measurement with which to test the accuracy of this saturation technique.

For the case of the octahedral  $\text{SF}_6$  molecule, the infrared-active, triply degenerate,  $\nu_3$  mode located at  $939 \text{ cm}^{-1}$  in liquid  $\text{O}_2$  is the highest energy mode. Because its moment of inertia is much larger than that of  $\text{CH}_3\text{F}$ , the rotational bandwidth is significantly reduced. In the liquid environment, the rotational contribution to the  $\text{SF}_6$  vibrational linewidth is well described by a Debye diffusional model<sup>10</sup> rather than the much more nearly free rotation of the  $\text{CH}_3\text{F}$  molecule. In this Debye model, the rotational contribution to the linewidth is given simply by  $\Gamma = kT/3\pi cV\eta$ , where  $kT$  is the temperature (ergs),  $c$  is the speed of light,  $V$  is the molecular volume, and  $\eta$  is the solution viscosity (poise). Figure II-3 shows the measured linewidth as a function of  $T/\eta$  for  $\text{SF}_6$  dissolved in liquid  $\text{O}_2$ . The viscosity was varied by changing the temperature of the cryogenic liquid.<sup>11</sup> From the slope of the line in Fig. II-3 we obtain an estimated molecular radius of  $6.2 \text{ \AA}$ , in reasonably good agreement with the radius of  $5.5 \text{ \AA}$  derived from second virial coefficients.<sup>12</sup> The zero-temperature intercept of  $0.23 \text{ cm}^{-1}$  sets a lower bound of 46 psec on the time to transfer energy out of the  $\nu_3$  mode. Energy-transfer processes may be slower than this, but if they were more rapid a broader  $\text{SF}_6$  linewidth would result. Since some of the times obtained from the saturation measurements are of this same order, this linewidth bound has important implications on the model of energy flow within the  $\text{SF}_6$  molecule.

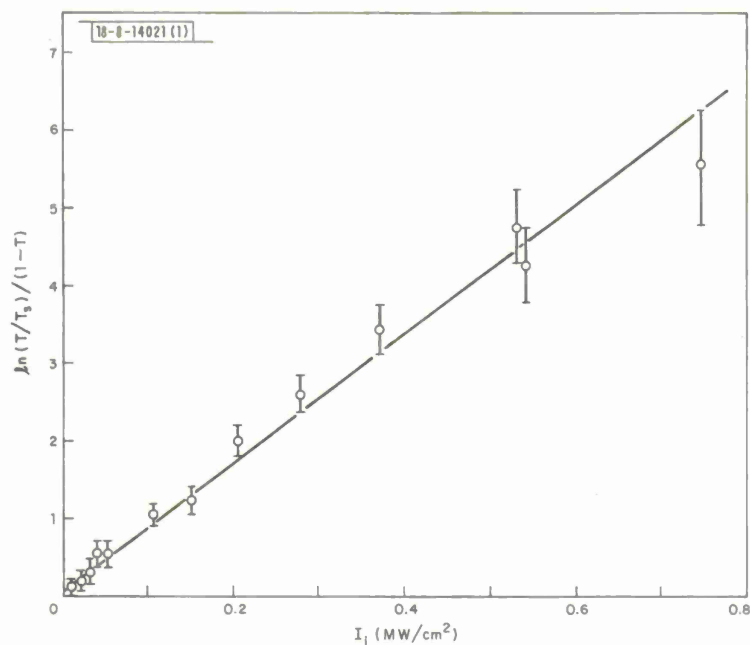


Fig. II-2. Plot of relative transmission [in the form  $\ln(T/T_s)/(1-T)$ ] of  $\text{CH}_3\text{F}$  in liquid  $\text{O}_2$ . ( $T = 77$  K,  $\ell = 6$  cm.) V-T time deduced from this plot is  $\tau \sim 150 \pm 50$  nsec.

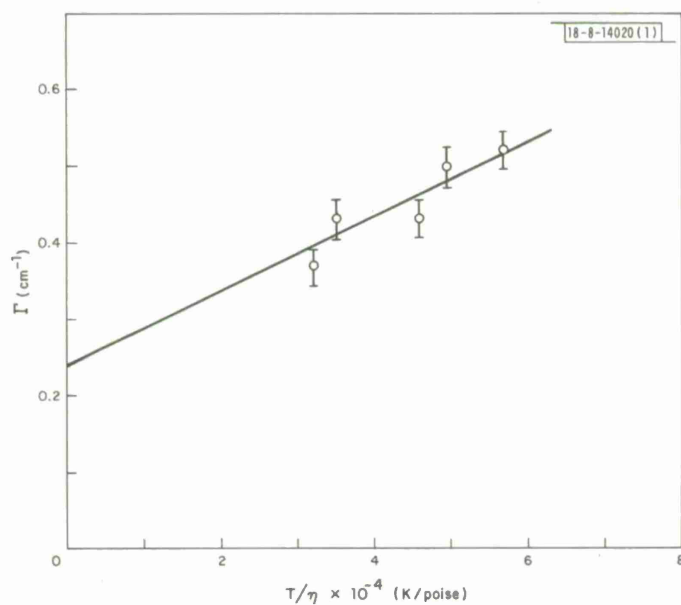


Fig. II-3. Dependence of infrared linewidth of  $\nu_3$  mode of  $\text{SF}_6$  on  $T/\eta$  ratio in liquid  $\text{O}_2$  solutions.

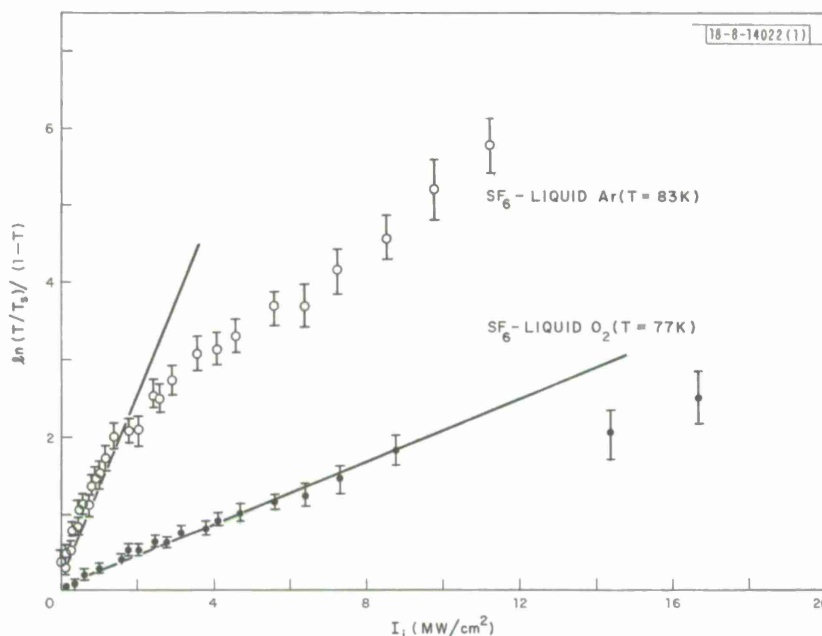


Fig. II-4. Plot of relative transmission [in the form  $\ln(T/T_s)/(1-T)$ ] of a  $3.3 \times 10^{15} \text{ cm}^{-3}$  solution of  $\text{SF}_6$  in liquid Ar and  $\text{O}_2$ . V-T times deduced from initial slopes of curves are  $\tau_{\text{Ar}} \sim 320 \pm 80 \text{ psec}$  and  $\tau_{\text{O}_2} \sim 54 \pm 15 \text{ psec}$ .

Figure II-4 shows the results of transmission measurements for  $\text{SF}_6$  dissolved in liquid Ar and  $\text{O}_2$ . Note that, in contrast to the  $\text{CH}_3\text{F}$  case, the measured curves are not simple straight lines but show significant deviations at higher input intensities. This arises because of significant excited-state absorption of the TEA laser radiation due to vibrational transfer processes which populate the lower-lying  $\text{SF}_6$  modes and give rise to absorptions to longer wavelengths than the  $\nu_3$  fundamental. This effect has also been observed in gas-phase studies.<sup>13</sup> The lower intensity portions of the curves in Fig. II-4 give relaxation times analogous to those found for  $\text{CH}_3\text{F}$ . As expected from gas-phase data,<sup>5-7</sup> the relaxation rates are much faster in  $\text{SF}_6$ , with a time of  $54 \pm 15 \text{ psec}$  for liquid  $\text{O}_2$  and  $320 \pm 80 \text{ psec}$  for liquid Ar. The liquid  $\text{O}_2$  result is of particular interest since it is in rough agreement with the lower bound on the energy-transfer time out of the  $\nu_3$  mode obtained from the linewidth analysis discussed above. These measurements were taken with modelocked laser pulses; similar curves were obtained when the mode-locking structure within the TEA laser pulse was eliminated by means of a gain cell. This is expected, since the relaxation times were shorter than the duration of a spike within the modelocked pulse.

A quantitative analysis of the upper region of the curves must await a detailed model of inter-mode energy transfer in  $\text{SF}_6$  and a more complete experimental investigation of the excited-state absorption by means of double-resonance experiments. Preliminary results from these double-resonance experiments indicate that the induced absorption follows the temporal variation of the TEA laser pulse, as is consistent with the rapid relaxation times reported here, and extends to at least  $8 \text{ cm}^{-1}$  lower in energy than the  $\nu_3$  fundamental, the limit of our measurement. No induced absorption was found at energies higher than the  $\nu_3$  fundamental. It is

interesting to note that, even with the extremely rapid relaxation rates of  $\text{SF}_6$  in liquid  $\text{O}_2$ , it is possible to saturate the transition with a  $\text{CO}_2$  TEA pulse and obtain significant excited-state absorption. This result indicates that the prospects for laser-induced chemistry in these liquid media appear promising. The usual picture of energy transfer in complex molecules such as  $\text{SF}_6$  is that there is a relatively rapid V-V equilibration between  $\nu_3$  and a manifold of the other modes, followed by a slower V-T relaxation of this manifold. This model seems inconsistent with our results for  $\text{SF}_6$  in  $\text{O}_2$ , since our measurements indicate that the rate of energy flow out of the  $\text{SF}_6$   $\nu_3$  mode is identical to that of the overall decay back to the ground state. The rapid V-V model would necessitate a faster decay of the  $\nu_3$  mode energy as it equilibrates with the vibrational manifold, and hence a broadened infrared linewidth, and then a slower decay back to the ground state.

In summary, we have demonstrated that valuable kinetic information in the picosecond time domain can be obtained by relatively simple saturation experiments. Extension of these techniques to other molecular liquid systems will greatly enhance our relatively meager store of information on vibrational kinetics in simple liquids.

S. R. J. Brueck  
T. F. Deutsch  
R. M. Osgood

### C. MULTIPHOTON ABSORPTION PROCESSES IN POLYATOMIC MOLECULES

The multiphoton, collisionless dissociation of polyatomic molecules using a pulsed  $\text{CO}_2$  laser has generated considerable interest in the processes by which energy is deposited in these molecules.<sup>14</sup> Most models suggest that the dissociation occurs via two steps, the first being selective excitation to a vibrational level so high that the density of states between it and the dissociation limit is essentially continuous. The second step involves the nonselective absorption of enough infrared photons to dissociate the molecule.

We have previously reported on the use of the pulsed acoustic spectrophone technique to measure the deposition of energy in cooled  $\text{SF}_6$  by a  $\text{CO}_2$  TEA laser as a function of laser frequency.<sup>15</sup> The absorption spectrum of  $\text{SF}_6$  broadens substantially to the low-frequency side, and develops a second absorption peak at  $\text{CO}_2$  laser intensities of a few  $\text{MW}/\text{cm}^2$ . Similar measurements on  $\text{SF}_6$  at room temperature by Soviet workers also show such a broadening, but do not reveal the structure observed at low temperatures.<sup>16</sup> We have extended our work to measurements of the intensity dependence of the absorption cross section at different  $\text{CO}_2$  laser pump frequencies, as well as spectral measurements, at 145, 198, and 293 K. In addition, less-extensive absorption measurements have been performed on  $\text{CH}_3\text{F}$ ,  $\text{CCl}_4$ , and  $\text{SiF}_4$ .

The measurements were made using a collimated  $\text{CO}_2$  TEA laser beam with a diameter of 3.1 mm. The output pulse had a 180-nsec-wide peak (FWHM) and a 1- $\mu\text{sec}$ -long tail. The gas was contained in a double dewar having an optical path length of 5.8 cm. Dry ice and acetone mixtures at 198 K and liquid  $\text{CF}_4$  at 145 K were used as refrigerants. An electret condenser microphone suspended in the cell was used to detect the acoustic signal due to the pressure rise caused by heating of the gas in the cell when it absorbs energy from the  $\text{CO}_2$  laser beam. The laser intensity was kept low enough that no significant dissociation occurred.

Figure II-5 shows the normalized acoustic signal for  $\text{SF}_6$  at 293 K, obtained by dividing the acoustic signal by the incident energy, as a function of the incident-energy density for several  $\text{CO}_2$  pump lines. Since the acoustic signal is proportional to the absorbed energy, the normalized acoustic signal is also proportional to the energy absorbed per incident-energy flux, referred to

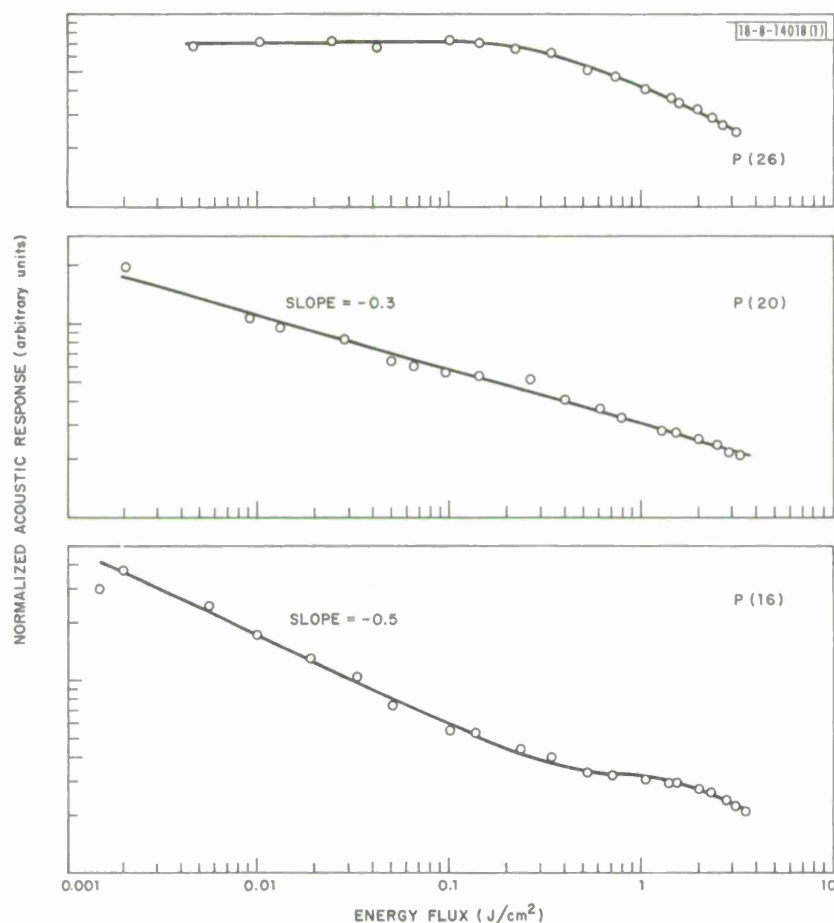


Fig. II-5. Normalized acoustic signal (acoustic signal divided by incident energy) as a function of energy flux for 0.25 Torr  $\text{SF}_6$  at 293 K for several  $\text{CO}_2$  laser lines.

here as normalized absorption. The normalized absorption for the P(16) line, which lies near the  $\text{Q}$  branch of the  $\nu_3$  mode, decreases with increasing energy, while for the P(20) and P(26) lines such saturation effects become progressively weaker. Similar behavior has been observed using a less-accurate calorimetric technique.<sup>17</sup>

The results of measurements on  $\text{SF}_6$  at 145 K, shown in Fig. II-6, are in striking contrast. While the absorption of P(16) still shows saturation effects for P(24) as well as for several other lines on the low-frequency side of the  $\text{SF}_6$   $\text{Q}$  branch, namely P(26) and P(28), the normalized signal increases with increasing energy. Calculations of the energy dependence of the normalized absorption have recently been made for  $\text{SF}_6$  at room temperature;<sup>17</sup> the low-temperature data presented here should provide a more sensitive test of this model.

The V-V (vibration-vibration) transfer time for  $\text{SF}_6$  at room temperature is  $1.5 \mu\text{sec-Torr}$ ;<sup>18</sup> hence, at typical  $\text{SF}_6$  pressures at 0.25 Torr, no V-V equilibration occurs during the 180-nsec laser pulse. If the pulse length becomes comparable to the V-V time, relaxation processes occurring during the pump pulse can alter the energy deposition processes. This is illustrated in Fig. II-7, which shows the acoustic signal from  $\text{SF}_6$  at 198 K as a function of frequency for  $\text{CO}_2$  laser pulses of equal energy, but different length. The long pulse had most of its energy



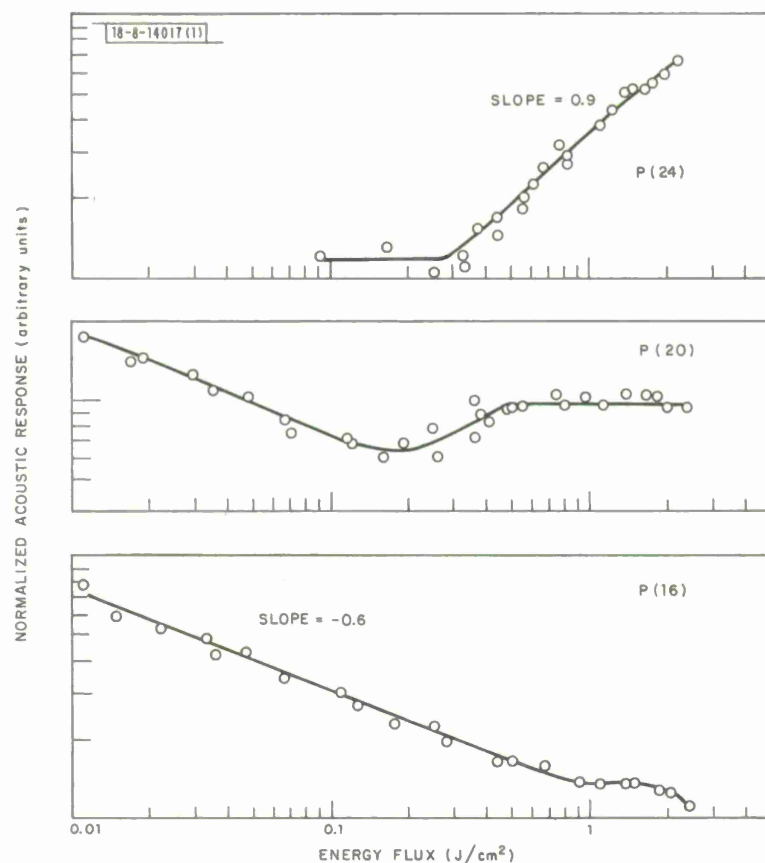


Fig. II-6. Normalized acoustic signal as a function of incident-energy flux for  $\text{SF}_6$  at 145 K ( $n = 9 \times 10^{15} \text{ cm}^{-3}$ ) for several  $\text{CO}_2$  laser lines.

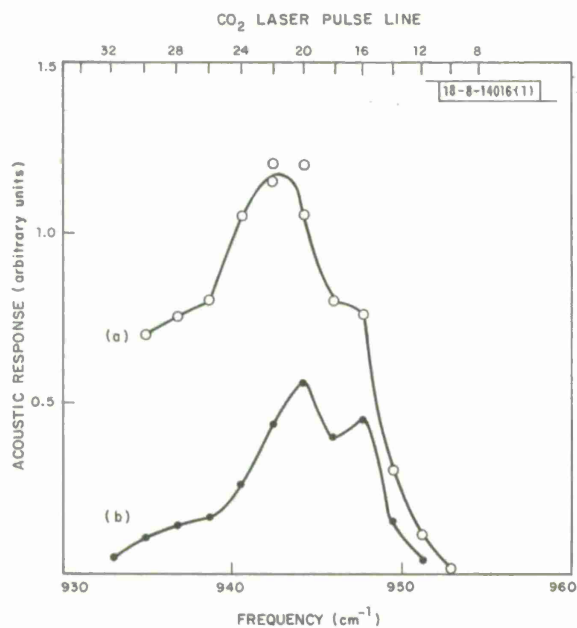


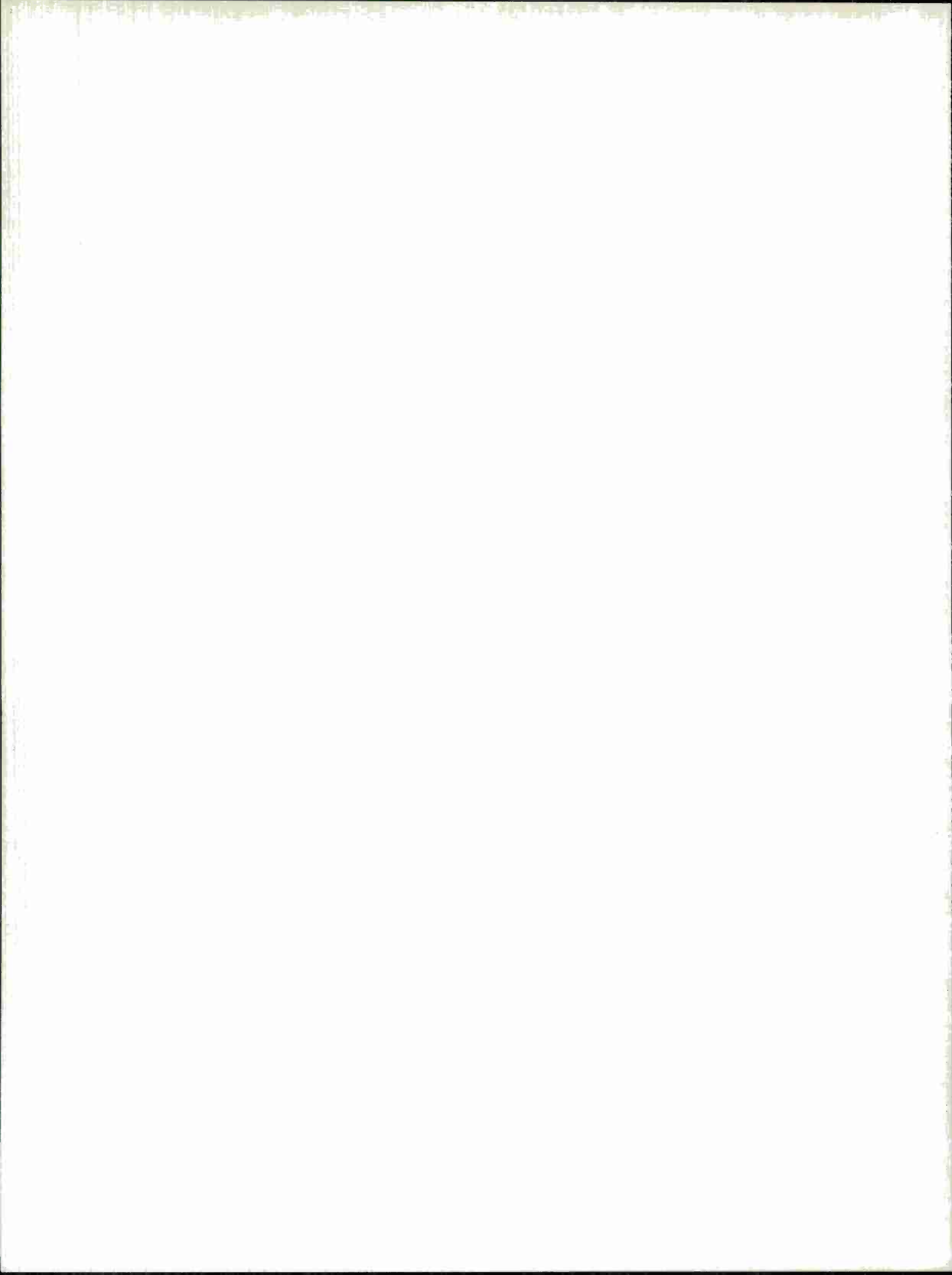
Fig. II-7. Spectral dependence of acoustic signal from  $\text{SF}_6$  at 198 K ( $n = 9 \times 10^{15} \text{ cm}^{-3}$ ) for (a) a 6- $\mu\text{sec}$ -long  $\text{CO}_2$  laser pulse, and (b) a 180-nsec-long pulse.

in a tail with a FWHM of 6  $\mu$ sec, while the short pulse was as described above. The acoustic absorption spectrum obtained with the long pulse shows a much more pronounced low-frequency tail as well as a greater absolute absorption. We believe that the enhanced tail is due to the formation of laser-induced hot bands. Such bands can be formed when the laser-excited  $\nu_3$  mode decays into lower-energy modes, producing hot bands (such as  $\nu_6 + \nu_3$ ) lying to the red of  $\nu_3$ .

T. F. Deutsch

#### REFERENCES

1. R. M. Osgood, Jr., Appl. Phys. Lett. 28, 342 (1976).
2. Solid State Research Report, Lincoln Laboratory, M.I.T. (1976:3), pp. 30-31, DDC AD-A034647.
3. R. V. Ambartsumian, Y. A. Gorokhov, V. S. Letokhov, and G. N. Makarov, JETP Lett. 21, 171 (1975).
4. J. L. Lyman, R. J. Jensen, J. Rink, C. P. Robinson, and S. D. Rockwood, Appl. Phys. Lett. 27, 87 (1975).
5. R. D. Bates, Jr., J. T. Knudtson, G. W. Flynn, and A. M. Ronn, Chem. Phys. Lett. 8, 103 (1971).
6. J. T. Knudtson and G. W. Flynn, J. Chem. Phys. 58, 1467 (1973).
7. E. Weitz and G. W. Flynn, J. Chem. Phys. 58, 271 (1973).
8. —————, Ann. Rev. Phys. Chem. 25, 275 (1974).
9. W. Kaiser and A. Laubereau in Tunable Lasers and Applications, edited by A. Mooradian, T. Jaeger, and P. Stokseth (Springer-Verlag, Berlin, 1976), pp. 207-217.
10. P. Debye, Polar Molecules (Reinhold, New York, 1929).
11. N. B. Vargaftik, Tables on the Thermophysical Properties of Liquids and Gases (Hemisphere Publishing Corporation, Washington, D.C., 1975).
12. J. O. Hirschfelder, C. F. Curtiss, and R. B. Bird, Molecular Theory of Gases and Liquids (Wiley, New York, 1954), p. 1111.
13. J. I. Steinfeld, I. Burak, D. G. Sutton, and A. V. Nowak, J. Chem. Phys. 52, 5421 (1970).
14. R. V. Ambartsumian, V. S. Letokhov, E. A. Ryabov, and N. V. Chekalin, JETP Lett. 20, 273 (1974).
15. Solid State Research Report, Lincoln Laboratory, M.I.T. (1976:2), p. 29, DDC AD-A030861/9.
16. V. N. Bagratashvili, I. N. Knyazev, V. S. Letokhov, and V. V. Lobko, Opt. Commun. 18, 525 (1976).
17. T. Cotter, submitted to J. Chem. Phys.
18. R. D. Bates, Jr., J. T. Knudson, G. W. Flynn, and A. M. Ronn, Chem. Phys. Lett. 8, 103 (1971).





### III. MATERIALS RESEARCH

#### A. ZIRCONIA MEMBRANES FOR HIGH-TEMPERATURE ELECTROLYSIS CELLS

Zirconia ( $\text{ZrO}_2$ ) stabilized with calcia ( $\text{CaO}$ ) or yttria ( $\text{Y}_2\text{O}_3$ ) is an effective solid electrolyte for oxygen-ion transport, with electrical conductivity values exceeding  $0.1 (\Omega \text{ cm})^{-1}$  at temperatures above  $800^\circ\text{C}$ . Use of this material should make it possible to produce hydrogen efficiently by means of high-temperature electrolysis cells, in which the transport of oxygen through stabilized-zirconia tubes or membranes under the influence of an applied voltage results in the dissociation of steam into oxygen and hydrogen. Efficient production of electric power should also be possible by combining such cells with low-temperature hydrogen-oxygen fuel cells in an electrochemical power cycle.<sup>1,2</sup>

Although high-temperature electrolysis cells utilizing zirconia tubes have been successfully fabricated and tested,<sup>3,4</sup> the basic design of these cells leads to a number of significant difficulties, including reliability problems arising from thermal incompatibility between the various materials used in cell construction, and high cell resistance resulting because the very thin metal electrodes applied to the zirconia tubes are used as the primary collectors of electric current. To overcome these disadvantages we have developed a flat-plate design in which the cells are constructed by vertically stacking a series of basic units, each consisting of a thin zirconia ceramic disk with a corrugated "egg crate" surface sandwiched between two thick metal plates. Models illustrating a basic unit and a complete cell are shown in Figs. III-1 and III-2, respectively. The metal plates hold the zirconia ceramic in compression for maximum strength and serve as current collectors, sealing gaskets, and heat-exchange fins. During electrolysis, steam entering the cell passes between the zirconia disk and one of the metal plates, gradually being converted to hydrogen as oxygen ions are transported to the other side of the disk, where they are discharged to form a stream of oxygen gas that passes between the disk and the other metal plate. Distribution ports for the entrance and exit of the gases are fabricated into the ceramic wherever required.

Because of the modular construction that is an inherent feature of the new design, it should be possible to produce high-performance electrolysis cells at relatively low cost. To achieve this objective, it is essential to have the capability of fabricating stabilized-zirconia membranes of the required size, shape, strength, and electrical properties. Since the preparation of thin, planar zirconia components has not been carried out previously, we have initiated the development of ceramic techniques for this purpose. By utilizing a procedure similar to the "green sheet" technology employed to produce alumina substrates for integrated circuit applications, we have succeeded in fabricating zirconia disks such as those shown in Fig. III-3. Although the mechanical and electrical properties of the disks have not been studied in detail, it appears that fabrication techniques based on this approach can yield satisfactory membranes for high-temperature cells.

The first step in the present procedure is to prepare a slurry of micrometer-size, yttria-stabilized-zirconia powder, plastic binder, plasticizer, and deflocculant in an organic solvent. A thin, uniform layer of the slurry is spread on a glass plate, where it is allowed to dry at room temperature to form a rubbery green sheet about 0.05 cm thick. This sheet is sufficiently rigid to be cut into disks and deformed into the egg-crate pattern shown in Fig. III-3. After being

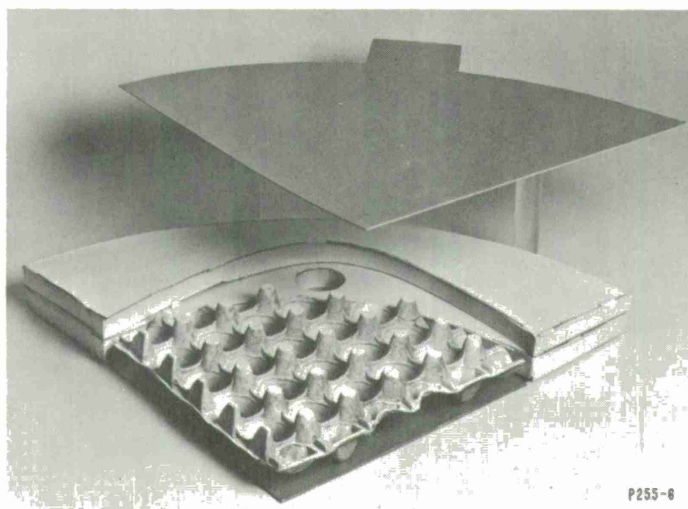


Fig. III-1. Model of basic flat-plate unit, consisting of stabilized-zirconia membrane with egg-crate surface sandwiched between two metal plates, for high-temperature electrolysis cell.

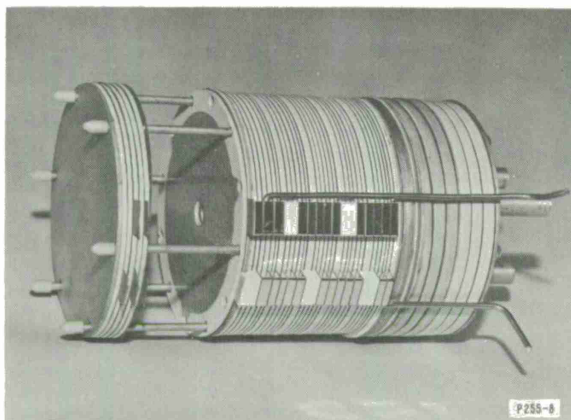


Fig. III-2. Model of assembled high-temperature electrolysis cell.

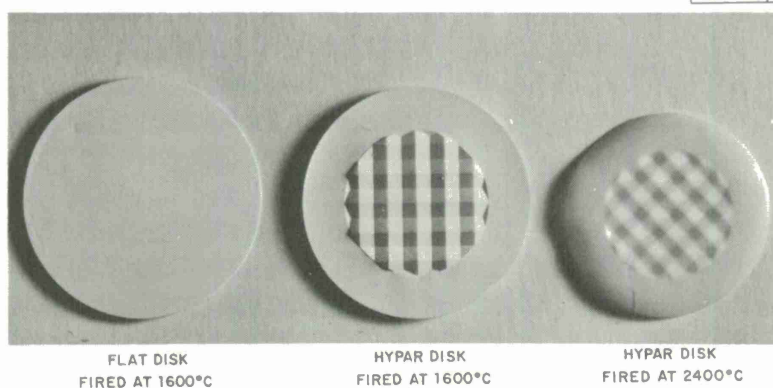


Fig. III-3. Zirconia membranes fabricated by green-sheet technique.

Fig. III-4. Cell for testing zirconia membranes and metal-zirconia seals.



shaped, it is converted to a bisque ceramic by firing in air at  $1600^{\circ}\text{C}$  for about 12 hr, which burns off the organic materials. In the bisque stage, the disk can be ground to final tolerance, after which it is converted to a high-density, impervious membrane by firing in a reducing atmosphere at  $2200^{\circ}\text{C}$  for about 12 hr. At this stage, the material has been darkened by reduction, but it becomes translucent after a final firing in air at  $1600^{\circ}\text{C}$  for 1 hr.

The flat-plate cell design also requires gas-tight compression seals to be made between the zirconia membranes and the supporting metal plates. A cell that has been built for testing such seals, as well as the electrolytic performance of the membranes, is shown in Fig. III-4. The seals are made with the metal "O"-rings shown, which are filled with high-pressure gas. In preliminary tests at  $1000^{\circ}\text{C}$  with a fused silica disk, a seal leaking less than  $1\text{ cm}^3/\text{hr}$  was achieved under a gas pressure of 2 atm.

T. B. Reed  
M. S. S. Hsu  
R. E. Fahey

#### B. SURFACE STATES ON $\text{SrTiO}_3$

In a continuing investigation of the role of semiconductor surface states in the photoelectrolysis of water, we have extended our previous *in situ* photoresponse measurements on  $\text{SrTiO}_3$  electrodes in photoelectrochemical cells. In an attempt to understand the differences observed<sup>5</sup> in the sign of the AC photoresponse to chopped ( $\sim 40\text{ Hz}$ ) radiation with photon energies less than energy gap, we have studied the time variation of the current response to light exposures as long as several minutes in duration. Such exposures to below-bandgap radiation produce large, slow photocurrent signals that peak in amplitude when the  $\text{SrTiO}_3$  electrode is biased sufficiently negative for the energy bands to become nearly flat but not enough for  $\text{H}_2$  to be evolved by photoelectrolysis. [A similar effect has recently been reported for  $\text{TiO}_2$  (see Ref. 6).] For an electrolyte pH of  $\sim 10$ , this occurs for a bias of  $\sim -0.9\text{ V}$  relative to the standard calomel electrode (SCE).

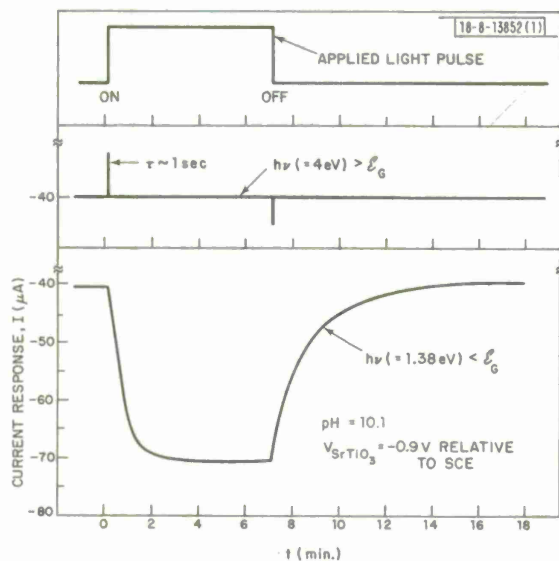


Fig. III-5. Current response of  $\text{SrTiO}_3$  electrode to monochromatic light for electrode bias of  $-0.9 \text{ V}$  relative to SCE and electrolyte  $\text{pH} = 10.1$ .

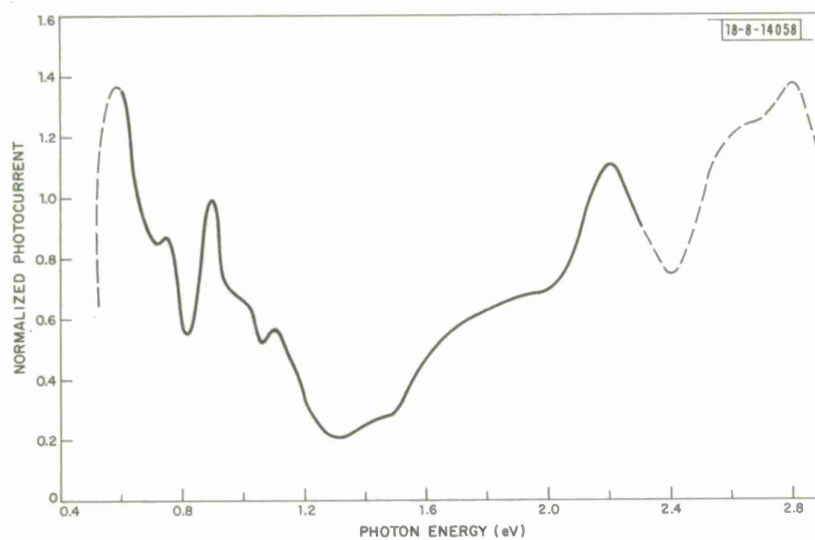


Fig. III-6. Photon-energy dependence of normalized photocurrent response of  $\text{SrTiO}_3$  electrode under conditions of Fig. III-5. Because of slight drift and low incident light intensity, values indicated by dashed lines are averages with estimated error of  $\pm 30$  percent.



Typical results under these bias conditions, obtained for an exposure of about 7 min. to monochromatic light of constant intensity, are given in Fig. III-5. The upper curve shows the light intensity in arbitrary units, while the middle and lower curves show the current as a function of time for exposure to photons of above- and below-bandgap energy, respectively. The response to above-bandgap photons consists primarily of two short current pulses, with time constants of the order of a second, which make the current less cathodic when the light is turned on and more cathodic when it is turned off. This response, which has the characteristic form associated with charging and discharging a capacitance, probably results from perturbing the Helmholtz double layer in the solution adjacent to the electrode. Of more interest is the response to below-bandgap radiation, which results in a cathodic photocurrent with time constants of the order of minutes.

Figure III-6 shows typical data for the spectral dependence of the steady-state photocurrent due to below-bandgap radiation. The observed structure, which is particularly prominent at lower photon energies, is associated with surface states in the energy gap rather than bulk states, since it is sensitive to the mechanical condition of the surface and also to the  $O_2$  concentration in the electrolyte. Both the dark cathodic current and the photocurrent are high when the solution is saturated with  $O_2$ . When  $O_2$  is eliminated by purging with  $N_2$ , the dark current decreases by about an order of magnitude and the photocurrent disappears.

Since the bias on the  $SrTiO_3$  electrode in these experiments is not sufficiently negative to permit photoelectrolysis, the photocurrent due to below-bandgap radiation must be associated with the  $O_2$  redox reaction. For an alkaline solution, this consists of the following reduction and oxidation:



which occur at the  $SrTiO_3$  cathode and platinum anode, respectively. The reduction results from the photoexcitation of electrons from the valence band to the surface states, from which they are transferred to the oxygen level of the electrolyte.

J. G. Mavroides  
J. A. Kafalas  
D. F. Kolesar

### C. X-RAY PHOTOEMISSION STUDY OF Sn-DOPED INDIUM OXIDE FILMS

Because thin films of Sn-doped  $In_2O_3$  are conducting and highly transparent to visible radiation,<sup>7,8</sup> they are useful for a variety of applications, including heat mirrors for solar collectors<sup>9</sup> and transparent electrodes for solar cells. The optical and electrical properties of these films are sensitive to preparation conditions. In order to obtain a better understanding of the factors determining these properties, we have studied the films by x-ray photoemission spectroscopy (XPS).

Films of Sn-doped  $In_2O_3$  between 300 and 5000 Å thick were deposited on CG 7059 glass substrates by RF sputtering from a 12.7-cm-diameter, hot-pressed target of  $In_2O_3$  containing 9 m/o  $SnO_2$  (see Ref. 8). Films of undoped  $In_2O_3$  and  $SnO_2$  were deposited by similar procedures, using hot-pressed targets of these materials. XPS measurements were made with a McPherson

apparatus. The specimens were irradiated with Mg  $K_{\alpha}$  x-rays with an energy of 1254 eV, and chemical binding energies were obtained by subtracting the kinetic energies of the photoelectrons from this incident energy. Experimental uncertainties in the binding-energy determinations are about  $\pm 0.10$  eV. Most of the measurements were performed on as-grown surfaces, but a few were made on films that had been sanded in dry  $N_2$  gas on either SiC or  $Al_2O_3$  abrasive paper. Sanding rather than argon-ion sputtering was used to remove the as-grown surface in order to avoid the differential sputtering effects observed for this material system.<sup>8</sup>

Figure III-7 shows the binding energies of the In 3d levels measured for  $In_2O_3$  powder and for  $In_2O_3$  and Sn-doped  $In_2O_3$  films before and after sanding. The observed binding energies of the In  $3d_{3/2}$  and  $3d_{5/2}$  levels are essentially the same (444.5 and 452.1 eV, respectively) for these and all the other samples containing In. We conclude that the In peaks in all the samples are due to ions with the formal valence state  $In^{3+}$ .

Figure III-8 shows the Sn  $3d_{3/2}$  and  $3d_{5/2}$  binding energies measured for SnO,  $SnO_2$ , and  $Sn_3O_4$  powders, and for an  $SnO_2$  film. The two peaks have essentially the same shape and positions for the  $SnO_2$  powder and film. The binding energies for  $SnO_2$  are significantly lower than those for SnO, in agreement with published results,<sup>10</sup> while they are slightly greater than those for  $Sn_3O_4$ .

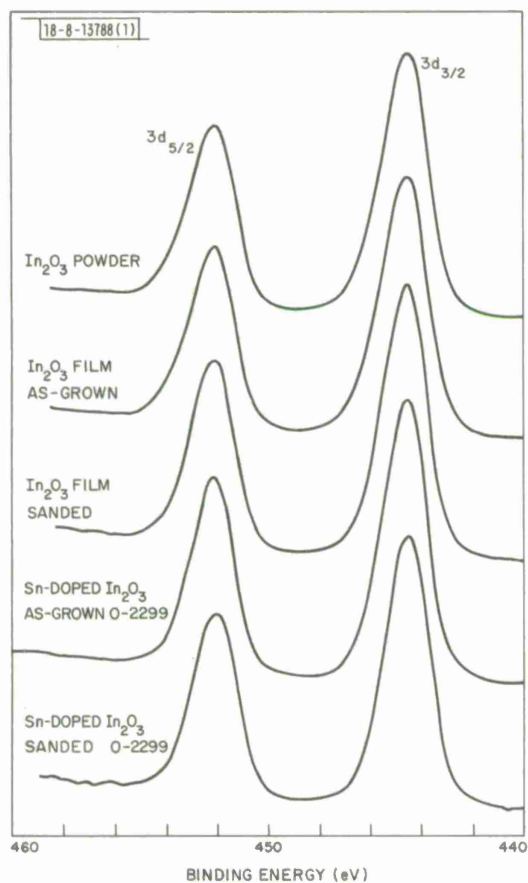


Fig. III-7. In  $3d_{3/2}$  and  $3d_{5/2}$  binding energies for  $In_2O_3$  powder and for  $In_2O_3$  and Sn-doped  $In_2O_3$  films before and after sanding.

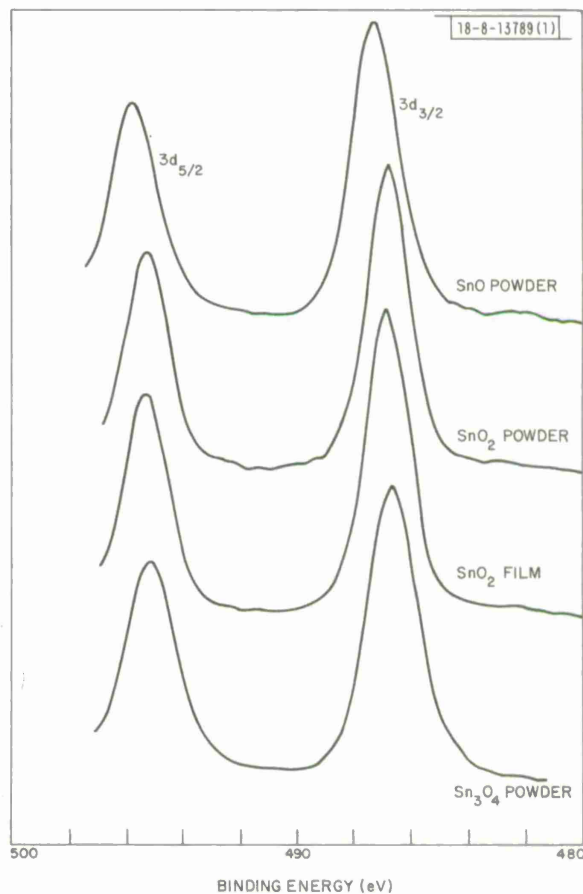


Fig. III-8. Sn  $3d_{3/2}$  and  $3d_{5/2}$  binding energies for SnO,  $SnO_2$ , and  $Sn_3O_4$  powders, and for an  $SnO_2$  film.

Fig. III-9. Sn  $3d_{3/2}$  and  $3d_{5/2}$  binding energies for two Sn-doped  $\text{In}_2\text{O}_3$  films before and after sanding.

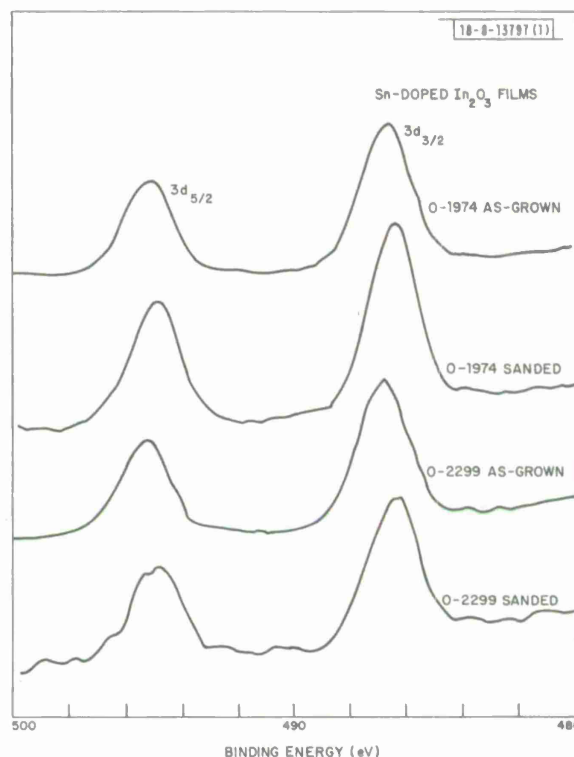


Figure III-9 shows the Sn  $3d_{3/2}$  and  $3d_{5/2}$  binding energies for two Sn-doped  $\text{In}_2\text{O}_3$  films prepared by sputtering at different power levels. The 2- $\mu\text{m}$ -thick, 100-W film 0-1974 had a visible transmission of less than 20 percent and a room-temperature resistivity of  $10^{-3} \Omega\text{-cm}$ . X-ray diffraction studies on similar films showed, in addition to  $\text{In}_2\text{O}_3$  peaks, the presence of weak  $\text{Sn}_3\text{O}_4$  peaks.<sup>8</sup> For the as-grown surface, the Sn binding energies are the same as those for  $\text{Sn}_3\text{O}_4$  powder. After sanding, these energies decrease by  $\sim 0.4$  eV, but the Sn/In ratio (i.e., the ratio of integrated areas under the Sn  $3d_{3/2}$  and In  $3d_{3/2}$  peaks) is essentially unchanged.

In contrast with film 0-1974, the 0.5- $\mu\text{m}$ -thick, 550-W film 0-2299 had a visible transmission of over 85 percent and a room-temperature resistivity of only about  $2.6 \times 10^{-4} \Omega\text{-cm}$ . X-ray diffraction showed only the  $\text{In}_2\text{O}_3$  phase.<sup>8</sup> The XPS Sn peaks for the as-grown surface have a composite structure. These peaks are similar in both shape and position to those obtained for a mixture of 5 m/o  $\text{SnO}_2$  and 5 m/o  $\text{SnO}$  with  $\text{In}_2\text{O}_3$  powder. Resolution of the Sn  $3d_{3/2}$  peak for the film into  $\text{SnO}_2$  and  $\text{SnO}$  peaks gave relative intensities with a 3-to-2 ratio. The peaks obtained after sanding also have a composite structure, but decreased by 0.4 eV. In addition, the ratio of the Sn  $3d_{3/2}$  to In  $3d_{3/2}$  integrated areas changes from 0.051 before sanding to 0.035 afterward, indicating that the as-grown surface has a higher Sn content than the bulk of the film. Similar results were obtained for a 0.6- $\mu\text{m}$ -thick, 600-W film that also had a visible transmission of over 85 percent and room-temperature resistivity of about  $2.6 \times 10^{-4} \Omega\text{-cm}$ .

Figure III-10 shows the oxygen 1s binding energies observed for the undoped  $\text{In}_2\text{O}_3$  film of Fig. III-7 and the Sn-doped  $\text{In}_2\text{O}_3$  films of Fig. III-9. The 0.4- $\mu\text{m}$ -thick  $\text{In}_2\text{O}_3$  film (sputtered at 550 W) had over 85-percent visible transmission and a room-temperature resistivity of about  $7 \times 10^{-4} \Omega\text{-cm}$ . As shown in Fig. III-11, the oxygen 1s peak for the as-grown surface has a composite structure that can be resolved into two Gaussian peaks  $\text{O}_\text{I}$  and  $\text{O}_\text{II}$ , separated by

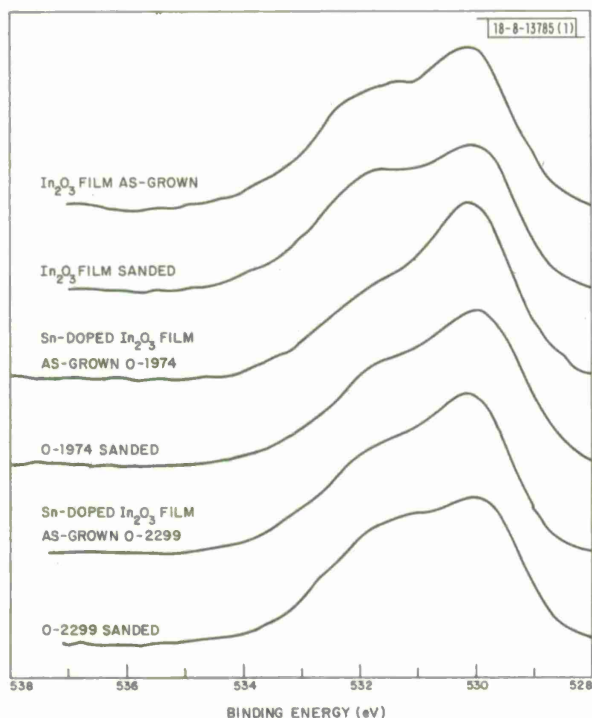


Fig. III-10. O 1s binding energies for an  $\text{In}_2\text{O}_3$  film and two Sn-doped  $\text{In}_2\text{O}_3$  films before and after sanding.

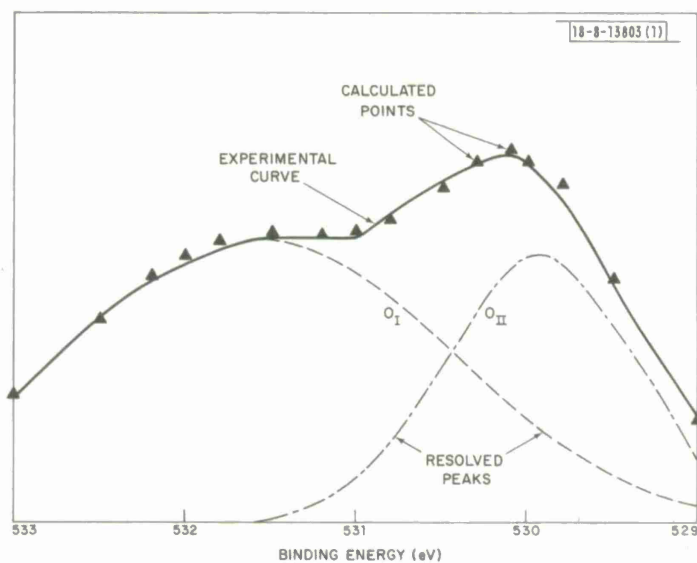


Fig. III-11. XPS peak for as-grown surface of an  $\text{In}_2\text{O}_3$  film resolved into  $\text{O}_I$  and  $\text{O}_{II}$  peaks. Calculated points were obtained by superposition of two resolved peaks.



about 1.5 eV, with an integrated intensity ratio of 52/48. After sanding, the 1s peak can again be resolved into  $O_I$  and  $O_{II}$  peaks, but with an intensity ratio of 57/43; the O/In ratio remains unchanged. Similar results were obtained for the Sn-doped  $In_2O_3$  films.

The present XPS investigation, together with our optical, electrical, and x-ray diffraction studies, has revealed two respects in which Sn-doped  $In_2O_3$  films with low visible transmission and low electrical conductivity differ from films with high transmission and high conductivity. In the dark films, the Sn concentration does not change significantly with depth, and an  $Sn_3O_4$ -like second phase is present. In the clear films, on the other hand, the Sn concentration is higher at the surface than in the bulk, and there is no evidence for an  $Sn_3O_4$ -like second phase. The formation of the second phase appears to be associated with the deposition of the dark films at much lower substrate temperatures.

J. C. C. Fan  
J. B. Goodenough

#### REFERENCES

1. M. S. S. Hsu, W. E. Morrow, Jr., and J. B. Goodenough, 10th Intersociety Energy Conversion Engineering Conference, University of Delaware, Newark, Delaware, 17-22 August 1975.
2. M. S. S. Hsu and T. B. Reed, 11th Intersociety Energy Conversion Engineering Conference, State Line, Nevada, 12-17 September 1976.
3. H. S. Spacil and C. S. Tedmon, Jr., J. Electrochem. Soc. 111, 1627 (1969).
4. Westinghouse Report 73-9E-COSHR-R1; Office of Coal Research Report 14-32-0001-1223 (April 1974).
5. Solid State Research Report, Lincoln Laboratory, M.I.T. (1976:2), p. 39, DDC AD-A030861/9.
6. H. Morisaki, M. Hariya, and K. Yazawa, Appl. Phys. Lett. 30, 7 (1977).
7. D. B. Fraser and H. D. Cook, J. Electrochem. Soc. 119, 1368 (1972).
8. J. C. C. Fan and F. J. Bachner, J. Electrochem. Soc. 122, 1719 (1975), DDC AD-A024234/7.
9. ———, Appl. Opt. 15, 1012 (1976), DDC AD-A027105/6.
10. W. E. Morgan and J. R. V. Wazer, J. Phys. Chem. 77, 965 (1973).



#### IV. MICROELECTRONICS

##### A. CHARGE-COUPLED DEVICES (CCDs): PROGRAMMABLE TRANSVERSAL FILTER

During the past quarter, a chip has been designed to add n-channel MOS shift registers and latch circuits to the original prototype CCD programmable transversal filter structure.<sup>1</sup> In the prototype device the tap weights were programmable as digital words which were controlled by switches external to the chip, but in the final device the digital words are to be stored on the chip in static logic devices. The analog input structure to the CCD sections has also been modified to make it controllable by the positive voltage levels of the logic devices.

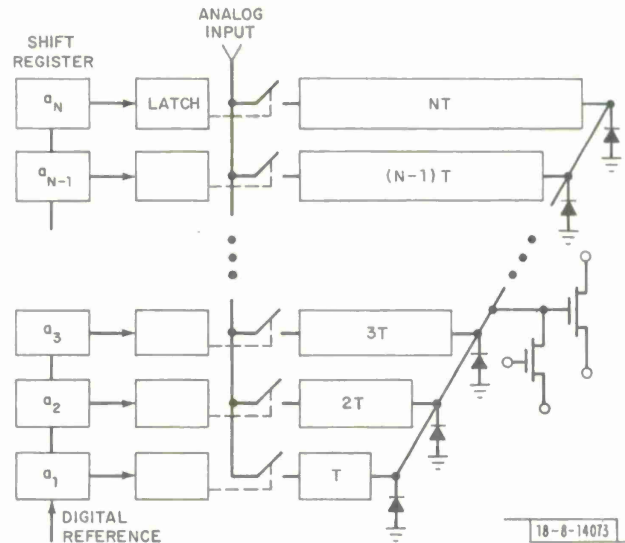


Fig. IV-1. Schematic illustration of a basic section of an N-stage CCD programmable transversal filter. Device convolves digital reference bits  $a_1, \dots, a_N$  with an analog input signal. Reference bits are introduced into shift register and stored in latch which, in turn, performs binary multiplication of analog signal and reference at CCD input.

The basic unit of the filter, shown in Fig. IV-1, consists of N CCD delay lines having from 1 to N cells. An N-stage shift register along the input end of the CCDs holds one bit of each of the N words representing the reference function or tap weights. A latch is included with the shift register as a buffer-store so that the reference bits can be transferred and held indefinitely, or until a new digital reference is clocked into the shift register. A simpler alternative is to use only a static shift register, but in this case the device is not usable during the N logic-clock periods needed to bring the new reference into place. The latch thus enables the change-over to a new reference to take place in about one clock period.

The state of each latch is used to control the analog input to the CCD and, in particular, to turn "on" or "off" the charge flow into the devices and, therefore, effect a multiplication of the analog input by a "zero" or "one." The CCD charge packets are collected at a common charge summing bus, and a conventional on-chip MOSFET output circuit serves as the preamplifier.

If the analog input signal is represented by time-samples  $x_n$  at time  $t_n$ , where  $t_{n+1} - t_n = T =$  clock period of the CCD, then the output signal  $y_m$  at time  $t_m$  is the convolution of the 1-bit reference words  $a_n$  and the sampled analog signal:

$$y_m = \sum_{n=1}^N a_n x_{m-n}$$

To achieve convolution with reference words each having  $M$  bits requires the use of  $M$  basic triangular units and the bit-weighting and summation of the output signals of the triangles as described previously.<sup>1</sup>

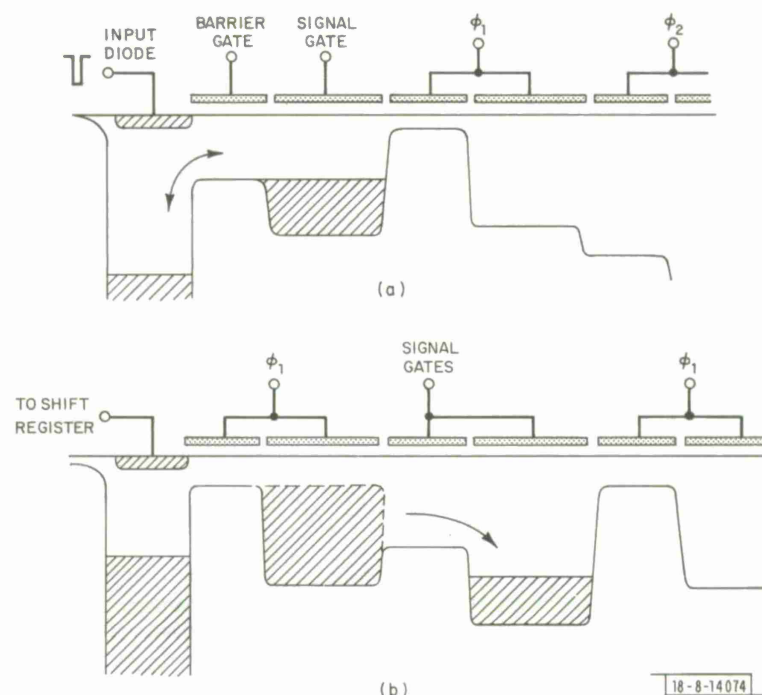


Fig. IV-2. (a) Conventional method known as "fill-and-spill" of introducing signals into a CCD. This method was used on prototype transversal filter. (b) New input method which allows binary multiplication of analog signal by means of a voltage on input diode. This method also eliminates a clocking waveform needed on input diode in (a).

In the prototype device, the analog input to each CCD used the conventional "fill-and-spill" method illustrated in Fig. IV-2(a). With a DC bias on the barrier gate and the signal applied to the signal gate, the input diode is pulsed low and then high again during the half-clock period when  $\phi_1$  is low. This leaves a charge packet residing under the signal gate which is proportional to the voltage difference between signal and barrier gates. For the prototype device, the binary multiplication was achieved by setting the bias on the barrier gate at a level that allowed charge filling of the signal gate (multiply by 1) or at a bias low enough to block the charge flow (multiply by 0). Because of the n-type buried channel, negative voltages (with respect to substrate) were required on the barrier gates to achieve the required control of the charge flow. This presents a problem since only positive voltages are available from n-channel MOS logic for

controlling this gate. A possible solution is a modified fill-and-spill described by Haken<sup>2</sup> and illustrated in Fig. IV-2(b). Here, an extra  $\phi_1$  cell is placed between the signal gate and the input diode. With the input diode at a logic LOW level of a few volts, the  $\phi_1$  well can scoop up a full well of charge and deliver a fraction of it to the well under the second signal gate. The quantity of charge transferred is proportional to the voltage difference between the signal and the low state of  $\phi_1$ . With a logic HIGH level of sufficient voltage on the input diode, charge will not flow into the  $\phi_1$  well when the latter is in its high state. An additional attractive feature of this method is that the clock pulse on the input diode [shown in Fig. IV-2(a)] is not needed.

Fabrication of a test chip similar to the original prototype devices but with the addition of 32-stage static shift registers, latches, and the new input structure to the CCD delay lines will require that the n-MOS logic device n<sup>+</sup> diffusions about the channel stops in order to maintain a compact structure. This will, in turn, require careful control of the p<sup>+</sup> channel-stop doping in order to achieve both high diode breakdown and high threshold voltage over the thick field oxide. Experiments are under way on test structures to determine suitable values of channel-stop ion-implantation doses and field-oxide thickness.

B. E. Burke  
A. M. Chiang  
D. L. Smythe

## B. CHARGE-COUPLED DEVICES: IMAGERS

Electrical characterization of the first of the 100- × 400-cell CCD imaging devices to be fabricated for the Ground Electro-Optical Deep Space Surveillance (GEODSS) Program [see Ref. 1, p. 53] has begun. The time constants and densities of two trap levels thought to be responsible for transfer inefficiency have been identified by using a technique based on sequentially injected electrical signals. The most prominent source of transfer loss is a trap level which appears to be the acceptor level of gold located near the middle of the band gap.

The 100- × 400-cell imager is arranged in the serial-parallel-serial configuration described previously (Ref. 1, p. 53). An electrical input to the output register is supplied so that this 405-bit, two-phase register can be tested separately. A technique<sup>3</sup> has been described whereby the emission time constants of bulk trap levels responsible for transfer inefficiency can be measured. The procedure consists of filling the trap levels by sending charge packets through the device, and following these by a series of empty charge packets during whose transit time the traps will partially empty. If a signal of size  $Q_s$  is then sent through the device, a charge loss  $\Delta Q_s$  will be observed due to the refilling of the traps. An expression for the loss  $\Delta Q_s$  in a two-phase device of M bits in which the measured signal has been preceded by  $n_z$  empty charge packets is:<sup>4</sup>

$$\Delta Q_s = 2qM(V_{st} + FV_{tr}) \sum_i N_{ti} \exp[-1/2f_c \tau_{ei}] \{1 - \exp[-n_z/f_c \tau_{ei}]\} \quad (IV-1)$$

where  $N_{ti}$  is the trap density of the i<sup>th</sup> species,  $\tau_{ei}$  is the emission time constant,  $f_c$  is the CCD clock frequency, and  $V_{st}$  and  $V_{tr}$  are the volumes occupied by the charge packet under the storage and transfer gates, respectively. The filling probability F results from the fact that the charge flow and trapping dynamics are different under the transfer gates than they are under the storage gates.

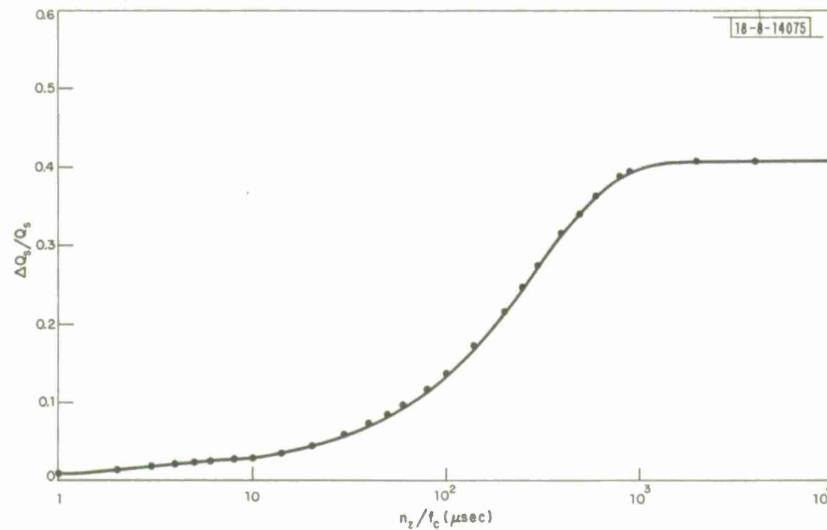


Fig. IV-3. Measured fractional charge loss  $\Delta Q_s/Q_s$  in a charge packet which has been preceded by  $n_z$  "zeros" or empty charge packets. Clock frequency  $f_c$  was 1 MHz in this case. A theoretical expression has been fitted to data indicating trap levels having emission time constants of 288 and 2.8  $\mu\text{sec}$ .

The results of this measurement on a device are presented in Fig. IV-3, where the relative charge loss  $\Delta Q_s/Q_s$  in the first signal charge packet is plotted against the time  $n_z/f_c$  elapsed between this charge packet and the last of the charge packets used to fill the traps. The clock frequency in this case was 1 MHz. Equation (IV-1) has been fitted to the data, and from this it is found that two trap levels having emission times of  $\tau_{e1} = 288 \mu\text{sec}$  and  $\tau_{e2} = 2.8 \mu\text{sec}$  are present. The estimated densities of these levels are  $3 \times 10^{12} \text{ cm}^{-3}$  and  $2 \times 10^{11} \text{ cm}^{-3}$ , respectively. Other reported measurements of this type have yielded levels having emission times of 275 and 0.3  $\mu\text{sec}$  (see Ref. 3) and 900 and 12  $\mu\text{sec}$  (see Ref. 4). The 900- $\mu\text{sec}$  level was tentatively identified as due to the acceptor level of gold located 0.54 eV from the conduction band. Although the emission time is a sensitive function of temperature, the temperature at which these measurements were made was not reported. In fact, a 15°C increase in device temperature would reduce the gold emission time constant by a factor of three, and bring the 900- $\mu\text{sec}$  measurement into agreement with our 288- $\mu\text{sec}$  result. Although in our case the ambient temperature was 29°C, a further complication is that the device itself is likely to be at a higher and spatially nonuniform temperature. For example, forward-bias measurements on a test diode located 70 mils from the CCD output showed a 10°C rise at that point due to power dissipated by the output MOSFET.

We conclude that the dominant charge-loss mechanism in our devices is likely due to the presence of gold at a concentration of about  $3 \times 10^{12} \text{ cm}^{-3}$ . An additional impurity at a much lower concentration and having a shorter emission time remains unidentified.

B. E. Burke

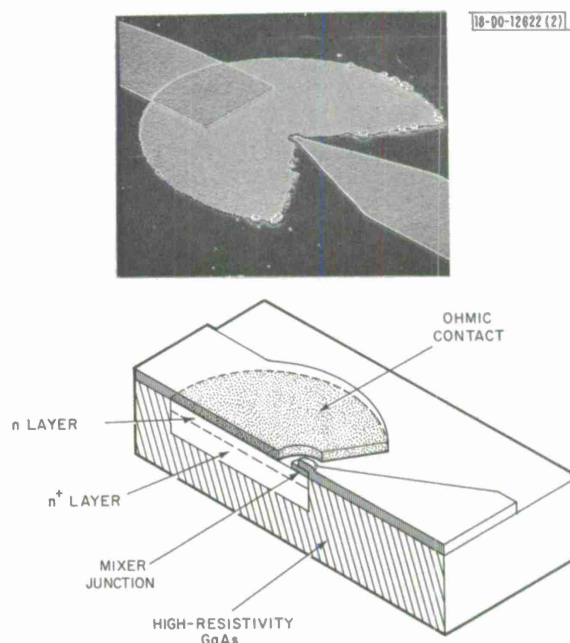
#### C. SURFACE-ORIENTED GaAs SCHOTTKY-BARRIER DIODES

Small, planar, surface-oriented Schottky diodes in which both terminals of the rectifying junction are on the same surface of the GaAs wafer have been fabricated for use in the submillimeter region. Conventional GaAs Schottky diode detectors operating in this region of the



spectrum require a small tungsten whisker to provide contact and to serve as a high-frequency antenna. In contrast, the single-sided geometry of the planar device lends itself naturally to an integrated circuit approach, enabling the connection of matched stripline antennas and IF filter networks. Although devices with this topography have been fabricated previously,<sup>5-7</sup> they have heretofore been restricted to frequencies below 100 GHz primarily because the relatively large area devices have led to high capacitance and low cutoff frequencies. Diodes with diameters as small as 2  $\mu\text{m}$  have been fabricated in our effort, permitting operation at submillimeter wavelengths for the first time.

Fig. IV-4. Bottom: planar diode as fabricated by growth of  $n$ - $n^+$  epitaxial layers on high-resistivity GaAs substrate. Top: scanning electron micrograph showing 2- $\mu\text{m}$  diode (small dot in center), ohmic contact establishing connection to the  $n^+$  layer of the diode, and two metal strip contacts.



The geometry of the device is shown in Fig. IV-4, together with a scanning electron micrograph of the completed device. To fabricate this structure, two layers of GaAs are epitaxially grown on semi-insulating substrates in a hydrogen transport  $\text{AsCl}_3$  vapor-phase system. The first layer ( $n^+$ ) is 3  $\mu\text{m}$  thick and has an  $n$ -type concentration of  $1 \times 10^{18} \text{ cm}^{-3}$ . The top layer ( $n$ ) is 0.5  $\mu\text{m}$  thick and has a concentration of  $1 \times 10^{17} \text{ cm}^{-3}$ . Sulfur ( $\text{H}_2\text{S}$ ) is used to dope both layers. Selective  $\text{Se}^+$ -ion implantation is then used to decrease the specific resistance of the Au-Ge alloyed ohmic contact. After the formation of the ohmic contact, the diode and ohmic contact areas are shielded by gold, and the wafer is proton bombarded converting the  $n$  and  $n^+$  layers to high-resistivity material in the bombarded regions. The sputter-deposited Pt/GaAs Schottky barrier is approximately 2  $\mu\text{m}$  in diameter. Each device is contacted by means of a stripline overlay pattern. A photograph showing an array of these devices on a completed wafer is shown in Fig. IV-5.

The forward current-voltage relationship of a typical device is shown in Fig. IV-6. This characteristic is quite similar to those of conventional Pt/GaAs diodes, with the knee of the non-linear region occurring at approximately 0.7 V. The  $n$ -factors of these devices (describing the deviation from ideal Schottky slope parameters) range from 1.2 to 1.4.

In preliminary experiments, a wafer fragment containing a number of diodes was placed on a probing apparatus under a microscope so that selected diodes could be contacted while being



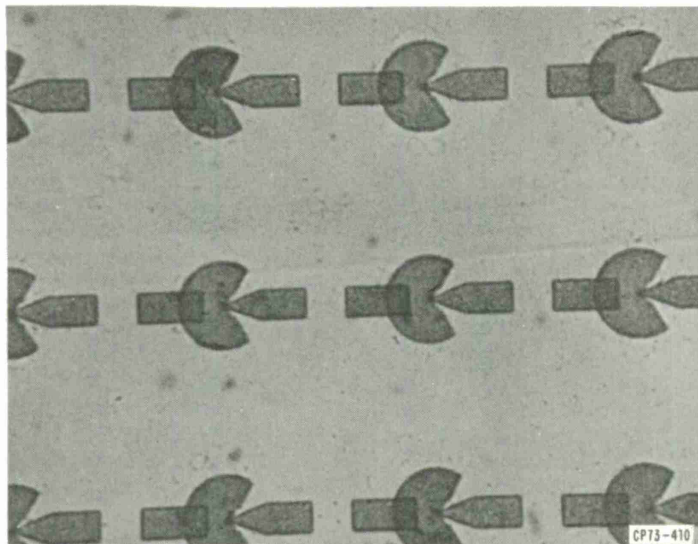


Fig. IV-5. Array of planar, surface-oriented diodes on GaAs wafer.

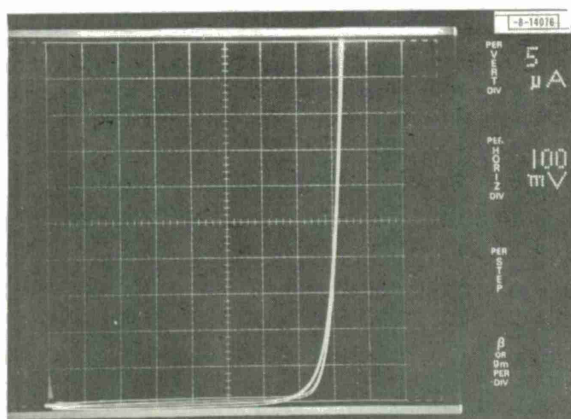


Fig. IV-6. Forward I-V characteristic of typical planar diode.

viewed optically. Various focusing arrangements were used to direct klystron or laser radiation onto the desired spot. In this manner, a responsivity of 40 V/W was obtained at 4 mm, and about 1 V/W at 337  $\mu\text{m}$ . These rudimentary results do not allow distinction between intrinsic frequency rolloff of the diodes and variations in coupling inefficiencies at different wavelengths.

In order to determine the fast-response capability of the diodes (i.e., demonstrate the non-linear interaction of high-frequency currents in the device), a number of mixing experiments were carried out. A single device was used which was thermo-compression bonded to a strip-line on an alumina substrate. First, a carcinotron with an output frequency at 333.95 GHz was mixed with the 5th harmonic of a V-band klystron operating at 66.79 GHz to produce a 90-MHz IF. The S/N obtained was greater than 30 dB. Next, beats were observed, again at a 90-MHz IF, between the 9th harmonic of a 74.21-GHz klystron signal and the 2nd harmonic of the carcinotron operating at 333.95 GHz. Mixing thus occurred at a frequency of 668 GHz.

Because of their topography, these diode devices can be fabricated in large numbers on single wafers which can be readily integrated with various forms of strip transmission line circuitry. Some of these concepts have already been successfully demonstrated in the case of the thin-film metal-oxide-metal structures.<sup>8</sup> In addition to stripline antennas, numerous other circuit elements can also be integrated with these devices either in a hybrid or monolithic fashion. Projected applications of this device involve their use in integrated circuit arrays which are required for large-area coherent detectors and submillimeter imaging devices. Preliminary development of simple antennas and arrays is in progress.

R. A. Murphy	C. D. Parker
C. O. Bozler	H. R. Fetterman
B. J. Clifton	J. P. Donnelly
W. T. Lindley	P. E. Tannenwald

#### D. DOUBLE-RETICLE METHOD OF ELIMINATING REPEATED DEFECTS IN MASKS

Quantitative measurements have been made of photoresist line width as a function of exposure time for the double-reticle technique<sup>9</sup> used to eliminate faults in chromium-coated master masks which arise from particulate contamination or emulsion defects in the 10X reticle. In this technique, the mask is exposed in the step-and-repeat camera with a reticle having nominal-sized geometries, and re-exposed with a second reticle having slightly oversized geometries. These measurements have been compared with similar measurements for the conventional single-reticle method in order to determine the effect on line width of exposing the mask with a second reticle.

Typical exposure-time test results for the single- and double-reticle methods are shown in Fig. IV-7, where each reticle has been exposed for the indicated length of time. (All experiments in this report were performed on photoplates coated with 0.1  $\mu\text{m}$  of AZ 1350 photoresist.) The optimum exposure time is less for the double-reticle case because some light from the oversized reticle finds its way into nominal-sized patterns from diffraction and scattering in the optical system, and from scattering and reflection from the chromium as shown in Fig. IV-8. The effect of reflection from a chromium coating can be determined by using low-reflective (black) chromium in order to minimize this source of stray light. The use of black chromium was found to reduce significantly the effect of scattered and diffracted light, as shown in the resist line width vs exposure-time curves of Fig. IV-9. For other photoplate materials the effects of scattering and diffraction can be determined from similar experiments, and the exposure time can be adjusted accordingly.

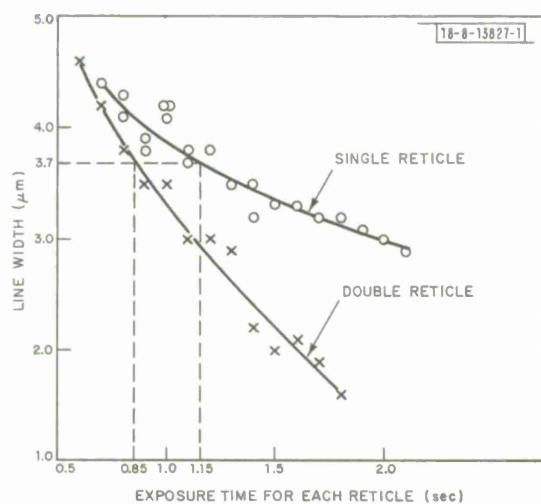


Fig. IV-7. Effect of second reticle on photoresist line width for chromium-coated photo-plates. Reduction in optimum exposure time is 26 percent for 3.7- $\mu\text{m}$  line. Lines on oversized reticle (10X) are 57  $\mu\text{m}$  wider than those on normal reticle.

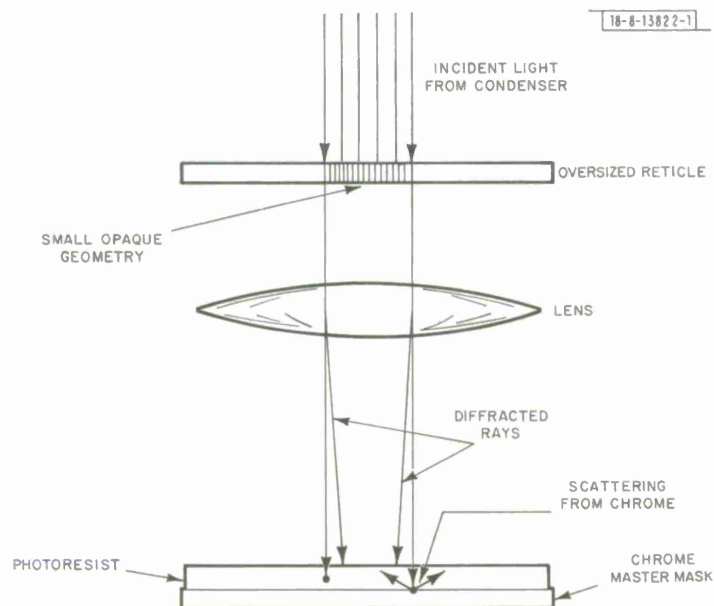
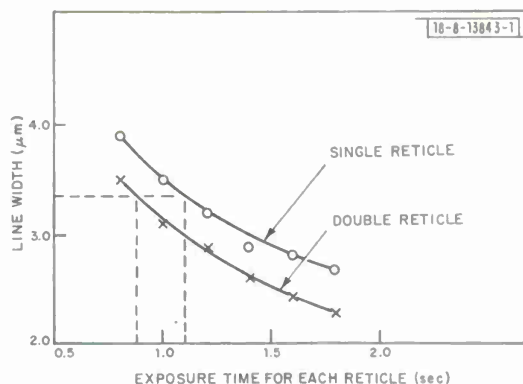


Fig. IV-8. Schematic representation of diffraction in lens and scattering from chrome. For simplicity, lens is shown as 1X.

Fig.IV-9. Effect of second reticle on photoresist line width for black-chromium photoplates. Optimum exposure time is reduced 18 percent. Normal reticle has 33.5- $\mu\text{m}$  lines, and oversized reticle has 84- $\mu\text{m}$  lines.



Also, we have observed that the total exposure time required depends upon the order in which the two reticles are used (as shown in Fig.IV-10). The 0.2- $\mu\text{m}$  difference in line width between the two curves for a 3.4- $\mu\text{m}$  line is a significant fraction of our line-width tolerance of 0.5  $\mu\text{m}$ . In order to eliminate this source of line-width variation, we always expose the two reticles in the same order. Exposing the normal reticle first requires a longer total exposure time than the reverse order of exposure, and consequently more consistent line widths because longer exposure times are easier to control.

The double-reticle technique with one nominal and one oversized reticle has limited usefulness for masks with small clear spaces such as those found on high-density positive or negative masks. Some 10X reticles have a significant fraction of their total area covered with clear areas smaller than the 50  $\mu\text{m}$  of total overhang necessary for successful application of this technique. Therefore, we have tried oversizing both reticles by a much smaller amount. The results of such an experiment are shown in Fig.IV-11 for exposure of a 4.0- $\mu\text{m}$  line. The curves

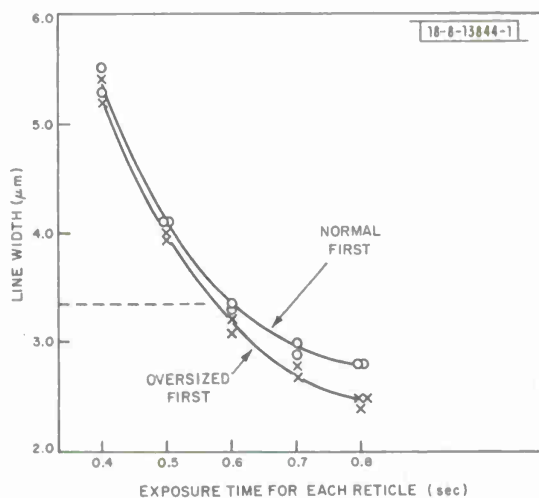


Fig.IV-10. Effect of order of exposure on photoresist line width for 3.4- $\mu\text{m}$  line on chromium. Difference in line width is 0.2  $\mu\text{m}$  or 6 percent. Lines on oversized 10X reticle are 51  $\mu\text{m}$  wider than those on normal reticle.

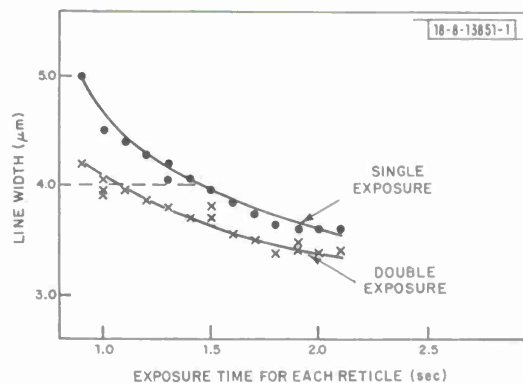


Fig.IV-11. Exposure time curves for double exposure on black chromium with same reticle. Top curve is for single exposure of 40- $\mu\text{m}$  lines on reticle. Bottom curve is for double exposure of 45- $\mu\text{m}$  lines. Reduction in optimum exposure time is 28 percent.

in this figure correspond to the curves in Figs. IV-7 and IV-9, except that in this case both reticles have been oversized by 5  $\mu\text{m}$  instead of one by 50  $\mu\text{m}$ . Note that the optimum exposure time is reduced by 28 percent for black chromium, which is comparable to the situation depicted by Fig. IV-7 for plain chromium.

The double-reticle technique with one oversized reticle has become a standard procedure for any of our work which requires reticles with unusually large clear areas. We have also fabricated successfully a limited number of masks using the technique of two slightly oversized reticles (see Fig. IV-11). We have almost eliminated the problems associated with gel slugs, and reticle cleaning is much less tedious. This technique tolerates a reasonable number of defects and particulates, and only the edges of the geometries on the normal reticle need be defect and contamination free. Although all the data presented here have been for exposure of AZ 1350 positive photoresist, the basic principle is also applicable to emulsion and negative photoresist.

However, the reader is cautioned not to attempt to draw more detailed quantitative conclusions from the data presented here because of the fact that these experiments were performed on a variety of different reticles with different feature sizes.

D. L. Smythe  
T. O. Herndon (Group 23)

#### REFERENCES

1. Solid State Research Report, Lincoln Laboratory, M.I.T. (1976:4), p. 56.
2. R. A. Haken, IEEE J. Solid-State Circuits SC-11, 189 (1976).
3. A. M. Mohsen and M. F. Tompsett, IEEE Trans. Electron Devices ED-21, 701 (1974).
4. R. W. Brodersen and S. P. Emmons, IEEE J. Solid-State Circuits SC-11, 147 (1976).
5. R. P. G. Allen and G. R. Antell, "Monolithic Mixers for 60-80 GHz," Proceedings of the 1973 European Microwave Conference, Paper A. 15.3 (September 1973).
6. W. C. Ballamy and A. Y. Cho, IEEE Trans. Electron Devices ED-23, 481 (1976).
7. E. J. Wood and A. A. Immorlica, "Monolithic Microwave GaAs Mixer Diodes," Technical Digest, International Electron Devices Meeting, December 1976, pp. 90-92.
8. J. G. Small, G. M. Elchinger, A. Javan, A. Sanchez, F. J. Bachner, and D. L. Smythe, Appl. Phys. Lett. 24, 275 (1974).
9. Solid State Research Report, Lincoln Laboratory, M.I.T. (1976:2), p. 50, DDC AD-A030861/9.



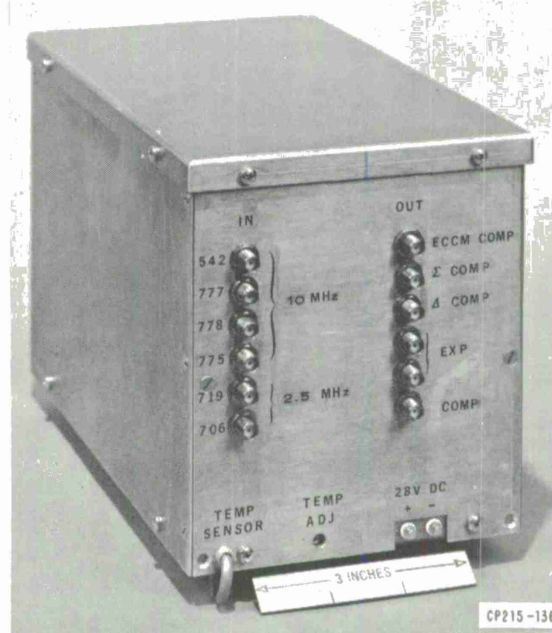
## V. SURFACE-WAVE TECHNOLOGY

### A. BISMUTH GERMANIUM OXIDE (BGO) REFLECTIVE-ARRAY COMPRESSORS

A second pulse expander/compressor subassembly for the MASR (Multiple-Antenna Surveillance Radar) system has been successfully fabricated. Delivery of this subassembly completes a two-phase program to develop dispersive delay lines on BGO in the RAC (reflective-array compressor) configuration. In the first phase, a narrowband (2.5-MHz bandwidth) sub-system consisting of a pulse expander and matching pulse compressor in a component oven was developed for the baseline MASR system. BGO was selected as the substrate material on which to fabricate these devices because the low surface-acoustic-wave (SAW) velocity combined with the foreshortening advantages of the folded RAC configuration allowed the required 125  $\mu$ sec of dispersion to be obtained on commercially available 15-cm substrates. The material and processing problems which were overcome in developing the first BGO RACs have been previously described.<sup>1,2</sup>

In the second phase of the program, dispersive delay lines with wider bandwidth (10 MHz) and larger dispersion (150  $\mu$ sec) were developed for the MASR monopulse system. These devices were incorporated in a single-component oven which also contained the devices previously developed for the baseline system. The final subassembly for the monopulse system consisting of six RAC devices mounted in a component oven is shown in Fig. V-1. Included in this total are

Fig. V-1. Component oven assembly containing two narrowband (2.5-MHz bandwidth, 125- $\mu$ sec dispersion) and four wideband (10-MHz bandwidth, 150- $\mu$ sec dispersion) BGO dispersive delay lines.



four wideband (10-MHz bandwidth, 150- $\mu$ sec dispersion) RAC units, namely, a waveform expander, a pair of pulse-compression lines for the monopulse receiver, and a third wideband pulse compressor for the ECCM guard channel. The remaining two devices are the narrowband (2.5-MHz bandwidth, 125- $\mu$ sec dispersion) pulse expansion and compression units. Because the temperature coefficient of delay of BGO is relatively large ( $\sim 130$  ppm/ $^{\circ}$ C), the component oven is necessary to stabilize the temperature and the overall delay through the subsystem.



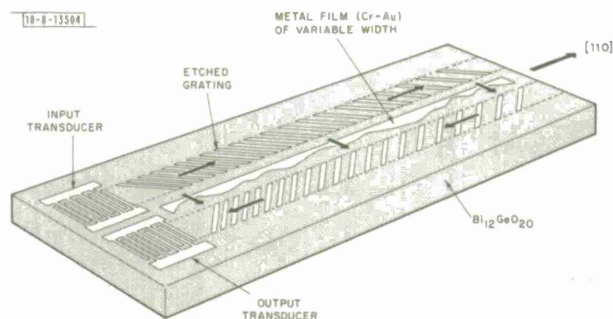


Fig. V-2. Schematic diagram of RAC. SAW propagation paths at different frequencies are indicated. Metal film between ion-beam-etched gratings provides phase compensation by selectively slowing surface wave.

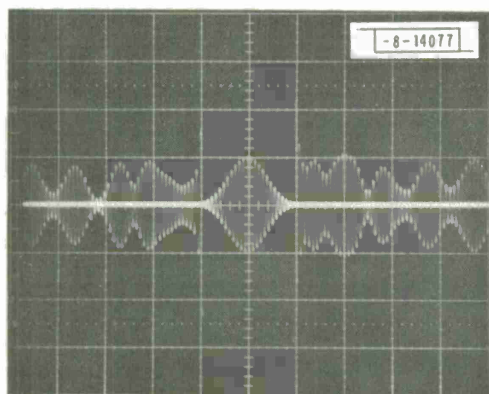
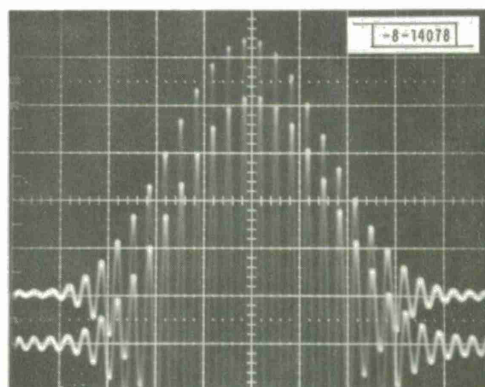


Fig. V-3. Compressed pulse and near-in sidelobe structure obtained with 10-MHz-bandwidth pulse expander and matched pulse compressor. For reference, center of figure shows central compressed pulse attenuated by 38 dB.

Fig. V-4. Compressed pulses obtained from pair of 10-MHz-bandwidth pulse compressors operating in parallel channels. Pulse compressors are precisely matched in both amplitude and delay. In this test, common input to both channels was an expanded pulse obtained from a single pulse expander.



RAC devices possess several characteristics which make them attractive for use as waveform-generation and signal-processing elements in a large-time-bandwidth radar system. In particular, pulse expanders can generate accurate large-time-bandwidth-product waveforms with high S/N ratios and low spurious responses, and matching pulse compressors can process the radar returns to yield high correlation gain, low time sidelobe, and large dynamic range. The stability of a SAW filter and its simplicity of operation in a pulse-expansion or compression circuit leads to stable system performance without the need for periodic tuning. In addition, the devices are small and therefore provide for very compact and lightweight subsystems. Near-ideal response is obtained from accurately designed RAC filters. The RAC configuration is schematically illustrated in Fig. V-2. The basic operation of this device has been described previously.<sup>3</sup>

The frequency response of the expansion lines is flat across the design bandwidth with a downchirp impulse response. The matching pulse compressors have an upchirp impulse response and are internally weighted to provide a Hamming frequency response. The results obtained on the more recently completed wideband units are summarized here; some initial results appear in an earlier report.<sup>4</sup> The narrowband devices are described elsewhere.<sup>1,2</sup> Midband CW insertion loss of the wideband RAC devices has been held to near 30 dB in order to provide pulse expanders with 60-dB S/N ratio and pulse compressors with a dynamic range of better than 80 dB. Additionally, direct electromagnetic feedthrough, which usually is the largest source of spurious signals in RAC devices, was suppressed to better than 90 dB below the input signal level.

Amplitude and phase errors of the individual RAC devices were reduced to low values consistent with design requirements that the remaining residual device errors contribute toward a worst-case compressed-pulse sidelobe level -35 dB below the compressed-pulse peak. Pulse-compression tests on cascaded expander and compressor pairs showed that, in general, the largest sidelobes were those adjacent to the mainlobe and were at the -35- to -38-dB level. Additional near-in sidelobes (those less than 5  $\mu$ sec from the mainlobe) were less than -40 dB. This near-in sidelobe structure, characteristic of the wideband devices, is shown in Fig. V-3. RAC devices have a unique geometrical effect which serves to strongly suppress far-out sidelobes.<sup>5</sup> This effect is evident in the wideband devices wherein the far-out sidelobes (those further than 5  $\mu$ sec from the mainlobe) quickly fall off to below -80 dB.

Two of the three wideband pulse compressors installed in each component oven assembly were selected for use in the monopulse channel. These were matched to provide equal time delay to the compressed-pulse outputs. To accomplish this, it was necessary to add approximately 50 nsec of delay by adding a length of semi-rigid coaxial cable to the signal path exhibiting the least time delay. The required lengths of cable are completely contained within the component oven assemblies. No degradation in compressed pulse sidelobe performance resulted from these corrections. The matched output waveforms obtained from each of the two devices designated for use in the monopulse channel are compared with one another in Fig. V-4. The waveforms are closely matched in both amplitude and time delay.

V.S. Dolat  
R.C. Williamson

#### REFERENCES

1. Solid State Research Report, Lincoln Laboratory, M.I.T. (1975:4), pp.60-62, DDC AD-A025489/6.
2. V. S. Dolat and R. C. Williamson, "BGO Reflective-Array Compressor (RAC) with 125  $\mu$ s of Dispersion," in 1975 Ultrasonics Symposium Proceedings (IEEE, New York, 1975), p. 390.
3. R. C. Williamson and H. I. Smith, IEEE Trans. Microwave Theory Tech. MTT-21, 195 (1973), DDC AD-772211/9.
4. Solid State Research Report, Lincoln Laboratory, M.I.T. (1976:3), pp. 53-54, DDC AD-A034647.
5. T. A. Martin, "Low Sidelobe IMCON Pulse Compression," in 1976 Ultrasonics Symposium Proceedings (IEEE, New York, 1976), p. 411.

UNCLASSIFIED

SECURITY CLASSIFICATION OF THIS PAGE (When Data Entered)

REPORT DOCUMENTATION PAGE		READ INSTRUCTIONS BEFORE COMPLETING FORM
1. REPORT NUMBER ESD-TR-77-44	2. GOVT ACCESSION NO.	3. RECIPIENT'S CATALOG NUMBER
4. TITLE (and Subtitle)  Solid State Research		5. TYPE OF REPORT & PERIOD COVERED Quarterly Technical Summary 1 November 1976 - 31 January 1977
		6. PERFORMING ORG. REPORT NUMBER 1977:1
7. AUTHOR(s)  Alan L. McWhorter		8. CONTRACT OR GRANT NUMBER(s)  F19628-76-C-0002
9. PERFORMING ORGANIZATION NAME AND ADDRESS Lincoln Laboratory, M.I.T. P.O. Box 73 Lexington, MA 02173		10. PROGRAM ELEMENT, PROJECT, TASK AREA & WORK UNIT NUMBERS  Program Element No. 65705F Project No. 649L
11. CONTROLLING OFFICE NAME AND ADDRESS Air Force Systems Command, USAF Andrews AFB Washington, DC 20331		12. REPORT DATE 15 February 1977
		13. NUMBER OF PAGES 56
14. MONITORING AGENCY NAME & ADDRESS (if different from Controlling Office)  Electronic Systems Division Hanscom AFB Bedford, MA 01731		15. SECURITY CLASS. (of this report)  Unclassified
		15a. DECLASSIFICATION DOWNGRADING SCHEDULE
16. DISTRIBUTION STATEMENT (of this Report)  Approved for public release; distribution unlimited.		
17. DISTRIBUTION STATEMENT (of the abstract entered in Block 20, if different from Report)		
18. SUPPLEMENTARY NOTES  None		
19. KEY WORDS (Continue on reverse side if necessary and identify by block number)		
solid state devices quantum electronics materials research microelectronics	surface-wave technology photodiode devices lasers laser spectroscopy	imaging arrays infrared imaging surface-wave transducers
20. ABSTRACT (Continue on reverse side if necessary and identify by block number)		
<p>This report covers in detail the solid state research work of the Solid State Division at Lincoln Laboratory for the period 1 November 1976 through 31 January 1977. The topics covered are Solid State Device Research, Quantum Electronics, Materials Research, Microelectronics, and Surface-Wave Technology. Funding is primarily provided by the Air Force, with additional support provided by the Army, ARPA, NSF, and ERDA.</p>		

Printed by  
United States Air Force  
Hanscom AFB, Mass. 01731